

# Spherically Averaging Ellipsoidal Galaxy Clusters in X-Ray and Sunyaev-Zel'dovich Studies: II. Biases

David A. Buote\* and Philip J. Humphrey

*Department of Physics and Astronomy, University of California, Irvine, 4129 Frederick Reines Hall, Irvine, CA 92697-4575, USA*

Accepted 2011 December 15. Received 2011 December 14; in original form 2011 September 29

## ABSTRACT

This is the second of two papers investigating the spherical averaging of ellipsoidal galaxy clusters in the context of X-ray and Sunyaev-Zel'dovich (SZ) observations. In the present study we quantify the orientation-average bias and scatter in observables that result from spherically averaging clusters described by ellipsoidal generalizations of the NFW profile or a nearly scale-free logarithmic potential. Although the mean biases are small and mostly  $< 1\%$ , the flattest cluster models generally have a significant mean bias; i.e., averaging over all orientations does not always eliminate projection biases. Substantial biases can result from different viewing orientations, where the integrated Compton- $y$  parameter ( $Y_{\text{SZ}}$ ) and the concentration have the largest scatter (as large as  $\sigma \sim 10\%$  for  $Y_{\text{SZ}}$ ), and the emission-weighted temperature ( $T_{\text{X}}$ ) has the smallest ( $\sigma \lesssim 0.5\%$ ). The very small scatter for  $T_{\text{X}}$  leads to  $Y_{\text{X}}$  and  $M_{\text{gas}}$  having virtually the same orientation biases. Substantial scatter is expected for individual clusters (up to  $\sigma \sim 8\%$ ) in the correlation between  $Y_{\text{SZ}}$  and  $Y_{\text{X}}$  in comparison to the small mean bias ( $\sigma \lesssim 1\%$ ) applicable to a random sample of clusters of sufficient size. For ellipsoidal NFW models we show that the orientation bias for the total cluster mass attains a minimum near the radius  $r_{2500}$  so that the spherically averaged mass computed at this radius is always within  $\approx 0.5\%$  of the true value for any orientation. Finally, to facilitate the accounting for orientation bias in X-ray and SZ cluster studies, we provide cubic polynomial approximations to the mean orientation bias and  $1\sigma$  scatter for each cluster observable as a function of axial ratio for the ellipsoidal NFW models.

**Key words:** X-rays: galaxies: clusters — X-rays: galaxies — dark matter — cosmological parameters — cosmology:observations

## 1 INTRODUCTION

Galaxy clusters are potent tools for cosmological studies (e.g., see reviews by Henry 2003; Schuecker 2005; Arnaud 2005; Voit 2005; Tozzi 2007; Allen et al. 2011). The redshift evolution of cluster baryon fractions supplements well-known geometrical cosmological constraints obtained by the cosmic microwave background radiation, supernova distances, and baryon acoustic oscillations. Important cosmological information complementary to these probes is provided by the growth of cosmic structure, which is manifested in a variety of ways for clusters, notably via the evolution of the cluster mass function. Since the hot intracluster medium (ICM) dominates the cluster baryons, X-ray observations are essential for measuring baryon fractions. They also provide one of the most effective means to measure the total gravitating mass for a cluster that obeys approximate hydrostatic equilibrium.

To obtain the most accurate constraints on the baryon fraction and total gravitating mass with X-ray observations requires obtaining accurate measurements of both the radial ICM density and temperature profiles out to a large fraction of the virial radius. These demanding requirements impose rather strict limits on the number of clusters which can be usefully analyzed with current data and data anticipated in the near future. Consequently, for cosmological studies with X-rays there is

\* E-mail: buote@uci.edu

much interest in using global scaling relations of quantities that act as mass proxies; e.g., the ICM temperature and gas mass measured from X-ray observations and the ICM pressure measured from either X-ray or Sunyaev-Zel’dovich (SZ) observations. Useful measurements of such proxies are possible for data of much lower quality and therefore may be applicable to much larger cluster samples than if detailed radial ICM profiles are needed. Moreover, even if the measurements of such mass proxies are of low quality, by averaging over large samples the impact of large statistical errors on measurements for individual systems is mitigated leading to precise cosmological constraints, which are accurate provided systematic errors also “average out” or are understood and controlled.

The hot ICM also traces feedback processes during cluster formation and evolution. For purely gravitational evolution the radial ICM entropy profile behaves as approximately  $r^{1.1}$  (e.g., Tozzi & Norman 2001; Voit et al. 2005), whereas feedback from an AGN and supernovas flattens the entropy profile mostly in the central regions (e.g., Tozzi & Norman 2001; Brighenti & Mathews 2001; Voit et al. 2002; Borgani et al. 2005; Romeo et al. 2006; Younger & Bryan 2007; McCarthy et al. 2008, 2010). Seemingly at odds with these theoretical expectations, recent X-ray studies of the Perseus and Virgo clusters measured entropy profiles that flatten near the virial radius (Simionescu et al. 2011; Urban et al. 2011). In addition, Simionescu et al. (2011) measure a gas fraction for Perseus that rises well above (over 50%) the cosmic mean baryon fraction. To reconcile these unanticipated results with the theoretical picture mentioned above, the authors of these studies postulate that near the virial radius the cluster ICM is substantially multiphase due to clumping from incompletely mixed material currently falling into the cluster – a hypothesis that subsequently has been given support by a cosmological simulation (Nagai & Lau 2011). In light of these results it is interesting that our recent *Chandra* and *Suzaku* study of the fossil group/cluster RXJ 1159+5531 out to the virial radius does not find a flat entropy profile and also yields a measurement of the baryon fraction that is very consistent with the cosmic mean value (Humphrey et al. 2011). A possible interpretation of these different results is that the magnitude of the gas clumping varies between clusters such that the most relaxed systems (like fossil groups) display the least amount of clumping. Of course, verifying this interpretation requires an accurate accounting of the important systematic errors involved with such measurements.

Deviations from hydrostatic equilibrium likely account for the largest systematic errors in X-ray measurements of cluster masses. Theoretical studies of clusters formed in hydrodynamical cosmological simulations find that such deviations can lead to mass errors ranging from a few percent up to  $\sim 30\%$  even for nominally relaxed clusters (e.g., Tsai et al. 1994; Evrard et al. 1996; Rasia et al. 2006; Nagai et al. 2007; Piffaretti & Valdarnini 2008; Vazza et al. 2011). The simulations typically find that non-thermal pressure generated by turbulent motions in the ICM is primarily responsible for the systematic underestimates of the masses. While the modest turbulent velocities associated with these mass biases are not strongly constrained by current spectral data (e.g., Schuecker et al. 2004; Sanders et al. 2011), the calorimeter to be operated on *ASTRO-H* (Takahashi 2011) should measure the amount of turbulent motions with novel precision, thereby providing a direct constraint on the accuracy of the hydrostatic equilibrium approximation and substantially reducing this source of systematic error for many clusters.

Arguably next in importance is the systematic error associated with the ubiquitous assumption of spherical symmetry, since it is well-known that clusters are not spherical. While this assumption is not required, it is the default standard for several reasons. First, the intrinsic shape and orientation of a cluster, even if it is assumed to be a triaxial ellipsoid, are not directly observable. Second, although promising approaches exist to constrain these properties indirectly through various combinations of X-ray, SZ, and lensing data (e.g., Zaroubi et al. 1998), they necessarily require more data and involve more complex modeling than if spherical symmetry is assumed. Finally, while it is generally recognized that for an individual cluster substantial error might be expected by assuming spherical symmetry (e.g., when viewing a highly flattened spheroidal cluster face-on), it is widely assumed (or hoped) that if it were possible to average such measurements over all possible cluster orientations, or rather average results over a statistically large cluster sample, that the effects of random projection orientations on cluster measurements should be eliminated entirely.

Over the years several theoretical studies have mentioned that observed ICM properties should not vary dramatically as a result of different intrinsic shapes and orientations. The pioneering study by Binney & Strimpe (1978) showed that even for spheroidal clusters highly inclined to the line-of-sight, deprojection assuming that the symmetry axis lies in the plane of the sky (effectively an assumption of spherical symmetry for large inclination angles) did not produce very large errors in the deprojected X-ray emissivity profile. It has been known since the first hydrodynamical cosmological simulation of a cluster that also simulated X-ray observations to quantify errors in the recovered mass, that significant ( $\sim 25\%$ ) errors could be expected from a combination of deviations from hydrostatic equilibrium and spherical symmetry (Tsai et al. 1994). More recently, cluster simulations have shown that significant scatter in the measurement of the integrated Compton- $y$  parameter ( $Y_{SZ}$ ) (proportional to the integrated ICM pressure) arises from effects due to non-spherical cluster morphology (e.g., White et al. 2002; Shaw et al. 2008; Krause et al. 2011). But precisely how much scatter arises from morphology alone is difficult to extract from such simulations; e.g., the large scatter in the relationship between measures of cluster morphology and deviations in the correlation between  $Y_{SZ}$  and mass (Krause et al. 2011).

It is therefore worth examining comparatively simple non-spherical models that effectively isolate the impact of assuming spherical symmetry on cluster measurements in X-rays or the SZ effect. Such examinations are quite uncommon in the literature, and when they do occur, they most often take the form of ancillary systematic error checks on X-ray cluster

measurements of the total mass and gas mass. For example, to examine the error from assuming spherical symmetry on their measurements of the gas mass in the cluster A 478, White et al. (1994) divided up the radial surface brightness profile from *ROSAT* into different azimuthal sectors, concluding that the masses were consistent between the different sectors within the estimated  $3\sigma$  statistical errors. This approach has also been applied to other systems, including the more recent study by Churazov et al. (2008) of *Chandra* observations of the low-mass clusters, M 87 and NGC 1399, in which they conclude errors of a few percent in their total mass measurements can be attributed to the assumption of spherical symmetry. Fabricant et al. (1984) and Buote & Canizares (1996b) noted in their studies of the intrinsic shapes of some clusters with *Einstein* and *ROSAT* that the spherically averaged total mass profiles obtained using both oblate and prolate spheroidal models were consistent, within the statistical errors, with the results obtained from assuming spherical symmetry. Buote & Canizares (1996b) also mentioned small ( $\sim 2\%$ ), but significant, errors on the gas mass if spherical symmetry is assumed. Finally, using spheroidal models Grego et al. (2000) estimate  $\sim 20\%$  systematic errors from assuming spherical symmetry on their SZ-derived estimates of the gas mass in A 370.

Piffaretti et al. (2003) and Gavazzi (2005) conducted the first studies dedicated to quantifying biases owing to the assumption of spherical symmetry in measurements of total cluster masses, in particular with respect to X-ray observations. Piffaretti et al. (2003) presented results for ten clusters observed with *ROSAT*. They modeled each cluster ICM as a tri-axial ellipsoid projected down its intermediate principal axis, with the major-axis profile described by the isothermal  $\beta$  model (Cavaliere & Fusco-Femiano 1976; Sarazin 1986). Their models indicated that the biases from assuming spherical symmetry were  $\lesssim 4\%$  for the total mass and  $\lesssim 5\%$  for the gas fraction. Gavazzi (2005) conducted a predominantly theoretical study of clusters modeled as spheroidal NFW (Navarro et al. 1997) mass distributions and isothermal ICM. To emphasize projection effects he focused on the special case of a cluster viewed down its symmetry axis (i.e., face-on). Like Piffaretti et al. (2003), generally he found mass biases of only a few percent owing to the assumption of spherical symmetry.

While significant biases from assuming spherical symmetry have been clearly demonstrated for particular intrinsic shapes and viewing orientations, the critical question of whether such biases completely “average out” when viewed from all directions remains unanswered. To address this important issue we compute theoretical orientation-average biases and scatter for ideal X-ray and SZ measurements as a function of the intrinsic shape of a cluster. We also consider several observables of interest to X-ray and SZ studies – concentration, total mass, gas mass, gas fraction, emission-weighted temperature,  $Y_X$ , and  $Y_{SZ}$  – and a wider range of models, including models with ICM temperature gradients. Finally, for a subset of models we provide cubic polynomial approximations to the mean orientation bias and  $1\sigma$  scatter of each observable that may be convenient for assessing the errors from assuming spherical symmetry in X-ray and SZ cluster studies

The paper is organized as follows. We define the ellipsoidal models in §2 and specify the default parameter values in §3. In §4 we describe the procedures to produce theoretical and observed spherically averaged observables. We present the results in §5 and our conclusions in §6. Our computations employ several of the analytical results for the deprojection and spherical averaging of ellipsoidal potentials derived in our companion paper (Buote & Humphrey 2011, hereafter Paper 1).

## 2 MASS MODELS

It is customary to approximate the isodensity contours of cluster dark matter halos formed in cosmological simulations by ellipsoids of constant shape and orientation (e.g., Jing & Suto 2002; Bailin & Steinmetz 2005; Allgood et al. 2006; Muñoz-Cuartas et al. 2011). While this is often a satisfactory approximation, more generally the isodensity contours of dark matter halos exhibit variations of shape and orientation with radius (e.g., Bailin & Steinmetz 2005; Allgood et al. 2006). To explore a variation of shape with radius in the mass distribution we also consider models where the isopotential contours have constant shape and orientation; e.g., the cored logarithmic potential (e.g., Binney 1981; Evans 1993). Here we extend the nomenclature of Kassiola & Kovner (1993) to three-dimensional systems by referring to models having ellipsoidal isodensity surfaces of constant shape and orientation as “Ellipsoidal Mass Distributions” and models with ellipsoidal isopotential surfaces of constant shape and orientation as “Ellipsoidal Potentials”, the latter of which are the focus of Paper 1.

Since each of these model types determines only how the flattening of the mass distribution varies with radius, the radial profile must also be specified. We will consider two different models: NFW (Navarro et al. 1997) and the cored logarithmic potential mentioned above. The NFW profile provides a good overall description of dark matter halos formed in cosmological simulations and also of the total mass profile inferred from X-ray observations of massive elliptical galaxies and clusters (e.g., see reviews by Arnaud 2005; Buote & Humphrey 2012, and references therein). Although the centers of dark matter halos are better represented by a Sersic/Einasto model (Navarro et al. 2004; Merritt et al. 2005), the additional accuracy at small radii is unimportant for our present study which focuses on global halo structure. Unlike the NFW model, the cored logarithmic potential is not motivated by cosmological simulations. Nevertheless, it also corresponds to the widely used isothermal  $\beta$ -model (Cavaliere & Fusco-Femiano 1976; Sarazin 1986) which is well-known to provide a good description of the radial X-ray surface brightness profiles of many galaxies and clusters.

Finally, we take the ICM to be a tracer population within a cluster, which is a reasonable approximation given that the

observed cluster gas fraction is  $\sim 10\%$  within the radius ( $r_{500}$ ) we investigate (e.g., Pratt et al. 2010). Although we ignore the self-gravity of the ICM we do examine how the gas mass (and gas fraction) implied by hydrostatic equilibrium in the single-component potential are affected by spherical averaging (see §4).

## 2.1 Spherical Models

We begin by presenting the density, enclosed mass, and gravitational potential for a spherically symmetric system for both the NFW and cored logarithmic potential models. This provides an opportunity to define some useful quantities that will be used throughout the paper and will serve as a convenient point of comparison for the ellipsoidal generalizations defined below in § 2.3 and § 2.4.

### 2.1.1 NFW

The NFW mass density profile,  $\rho(r) \propto r^{-1}(r_s + r)^{-2}$ , has two free parameters: (1) a normalization and (2) a scale radius ( $r_s$ ) denoting where the logarithmic slope of the density profile equals -2. It is conventional to replace these with the following related parameters. Define the concentration parameter,  $c \equiv r_\Delta/r_s$ , where  $r_\Delta$  is defined so that the average density of the halo with that radius equals  $\Delta$  times the critical density of the universe ( $\rho_{\text{crit}}$ ). Typically quoted values for  $\Delta$  range from 100-2500. For the other parameter, define  $M_\Delta$  to be the mass enclosed within  $r_\Delta$ . With these definitions, the NFW density, enclosed mass, and gravitational potential take the form,

$$\rho(\tilde{r}) = \frac{M_\Delta}{4\pi r_\Delta^3} \frac{c^3}{A(c)} \frac{1}{c\tilde{r}(1+c\tilde{r})^2}, \quad (1)$$

$$M(< \tilde{r}) = M_\Delta \frac{1}{A(c)} \left[ \ln(1+c\tilde{r}) - \frac{c\tilde{r}}{1+c\tilde{r}} \right], \quad (2)$$

$$\Phi(\tilde{r}) = -\frac{GM_\Delta}{r_\Delta} \frac{1}{A(c)} \frac{\ln(1+c\tilde{r})}{\tilde{r}}, \quad (3)$$

where,

$$\tilde{r} \equiv \frac{r}{r_\Delta}, \quad A(c) \equiv \ln(1+c) - \frac{c}{1+c}, \quad \frac{3M_\Delta}{4\pi r_\Delta^3} \equiv \Delta\rho_{\text{crit}}. \quad (4)$$

### 2.1.2 CORELOG (also Isothermal $\beta$ -model)

As befits its name, the cored logarithmic potential is defined by the form of its potential,  $\Phi = -(v_o^2/2) \ln(r_c^2 + r^2)$  (e.g., Binney 1981; Evans 1993; Binney & Tremaine 2008). Like the NFW model it has two free parameters: a normalization ( $v_o$ ) and a scale radius ( $r_c$ ), usually called a ‘‘core radius.’’ For consistency of presentation we redefine these parameters in analogy with that done for the NFW model above. That is, we define a concentration parameter,  $c \equiv r_\Delta/r_c$ , and mass,  $M_\Delta$ , where  $r_\Delta$  is again defined so that the average density within a sphere of that radius equals  $\Delta$  times the critical density. When expressed in terms of  $c$  and  $M_\Delta$  the cored logarithmic potential and derived quantities take the form,

$$\rho(\tilde{r}) = \frac{M_\Delta}{4\pi r_\Delta^3} (1+c^2) \frac{3+(c\tilde{r})^2}{[1+(c\tilde{r})^2]^2}, \quad (5)$$

$$M(< \tilde{r}) = M_\Delta (1+c^2) \frac{\tilde{r}^3}{1+(c\tilde{r})^2}, \quad (6)$$

$$\Phi(\tilde{r}) = -\frac{GM_\Delta}{2r_\Delta} \frac{(1+c^2)}{c^2} \ln\left(\frac{1+c^2}{1+(c\tilde{r})^2}\right), \quad (7)$$

where,  $\tilde{r}$  and  $M_\Delta$ , are defined as above (eqn. 4). We have chosen the arbitrary constant term in the potential so that  $\Phi = 0$  when  $r = r_\Delta$ . Henceforth we will refer to this model as the ‘‘CORELOG’’ model. In order to provide a sharper contrast with the NFW model, we will focus on the case  $c \gg 1$  so that  $\Phi \sim \ln(r)$ , corresponding to the singular isothermal sphere. It is noteworthy that eqn. (7) also corresponds to the potential of the isothermal  $\beta$ -model (Cavaliere & Fusco-Femiano 1976; Trinchieri et al. 1986), where the ICM density is assumed to obey,  $\rho_{\text{gas}} \propto (1+(r/r_c)^2)^{-3\beta/2}$ , and the factor outside the logarithm equals,  $-(3\beta/2)(k_B T/\mu m_a)$ , where  $T$  is the ICM temperature,  $k_B$  is Boltzmann’s constant,  $\mu$  is the mean atomic weight of the ICM, and  $m_a$  is the atomic mass unit.

## 2.2 Ellipsoidal Models – General Considerations

As in Paper 1 we consider an ellipsoid of principal axes  $a, b, c$  with axis ratios  $p_v \equiv b/a$  and  $q_v \equiv c/a$  satisfying  $0 < q_v \leq p_v \leq 1$ . When the ellipsoid is oriented so that  $a$  lies along the  $x$ -axis,  $b$  along the  $y$ -axis, and  $c$  along the  $z$ -axis, the ellipsoidal radius is defined by,

$$a_v^2 = x^2 + \frac{y^2}{p_v^2} + \frac{z^2}{q_v^2}. \quad (8)$$

For the ellipsoidal generalizations of the spherical NFW and CORELOG models we consider below, we will make use of the following quantities,

$$\tilde{a} \equiv \frac{a_v}{a_\Delta}, \quad \frac{3M_\Delta}{4\pi p_v q_v a_\Delta^3} \equiv \Delta\rho_{\text{crit}}, \quad (9)$$

where, in analogy to the spherical case,  $a_\Delta$  is defined so that the average density within an ellipsoid  $a_v = a_\Delta$  equals  $\Delta\rho_{\text{crit}}$ , and  $M_\Delta$  refers to the mass contained within that ellipsoid.

## 2.3 Ellipsoidal Potentials – EPs

For a detailed discussion of this model type we refer the reader to Paper 1. Briefly, we define an ellipsoidal potential (EP) model such that the gravitational potential is an ellipsoid of constant shape  $(p_v, q_v)$  and orientation; i.e.,  $\Phi$  depends only on  $a_v$ . For this model type one begins by specifying  $\Phi(a_v)$  and then deduces the mass distribution from it. The key advantage of an EP is that a simple, analytic form for  $\Phi$  can be adopted, enabling much faster computational evaluation than for ellipsoidal mass distributions (§2.4). A disadvantage is that when the potential is sufficiently flattened (the amount depending on how steep is the radial potential profile), the model can become unphysical in regions near the shortest principal axis; e.g., as manifested by negative values for the mass density (e.g., Binney & Tremaine 2008). However, since we primarily make use of the integrated mass profile, which is as well-behaved as for spherical analogs of  $\Phi$  (see Paper 1), localized peculiar features in the density profiles of EP models are not important for our investigation.

In Theorem 1 of Paper 1 we show that the mass enclosed within  $a_v$ ,  $M(< a_v)$ , is related to the the potential  $\Phi(a_v)$  in the same manner as the spherical  $M(< r)$  is related to  $\Phi(r)$ , with the introduction of a proportionality constant,

$$\eta(p_v, q_v) \equiv \frac{p_v q_v}{3} \left[ 1 + \frac{1}{p_v^2} + \frac{1}{q_v^2} \right], \quad (10)$$

which is of order unity. We emphasize that  $p_v$  and  $q_v$  define the shape of  $\Phi$  and the bounding surface for the calculation of  $M(< a_v)$  (and thus definition of  $M_\Delta$  below in §2.3.1 and §2.3.2), but the mass density distribution of an EP generally has smaller axis ratios (see §3) and is not strictly ellipsoidal.

We now define versions of the NFW and CORELOG models appropriate for EPs.

### 2.3.1 NFW-EP

We convert the spherical NFW model to an EP starting with the potential defined by eqn. (3) and letting  $r \rightarrow a_v$  and  $r_\Delta \rightarrow a_\Delta$ ,

$$\Phi(\tilde{a}) = -\frac{GM_\Delta}{a_\Delta} \frac{1}{A(c)} \frac{\ln(1+c\tilde{a})}{\tilde{a}}, \quad (11)$$

where  $c \equiv a_\Delta/a_{\text{scale}}$  and  $a_{\text{scale}}$  is an ellipsoidal analog of  $r_s$ . From this modified potential the mass profile is computed using eqn. (7) of Paper 1 to give,

$$M(< \tilde{a}) = M_\Delta \frac{\eta(p_v, q_v)}{A(c)} \left[ \ln(1+c\tilde{a}) - \frac{c\tilde{a}}{1+c\tilde{a}} \right], \quad (12)$$

and the density profile is computed from Poisson's equation which yields,

$$\rho(x, y, z) = \frac{M_\Delta}{4\pi a_\Delta^3} \frac{c^3}{A(c)} \frac{1}{(c\tilde{a})^2(1+c\tilde{a})} \times \left[ \frac{3+4c\tilde{a}}{1+c\tilde{a}} \frac{1}{a_v^2} \left( x^2 + \frac{y^2}{p_v^4} + \frac{z^2}{q_v^4} \right) - \left( 1 + \frac{1}{p_v^2} + \frac{1}{q_v^2} \right) + \frac{(1+c\tilde{a}) \ln(1+c\tilde{a})}{c\tilde{a}} \left[ \left( 1 + \frac{1}{p_v^2} + \frac{1}{q_v^2} \right) - \frac{3}{a_v^2} \left( x^2 + \frac{y^2}{p_v^4} + \frac{z^2}{q_v^4} \right) \right] \right]. \quad (13)$$

### 2.3.2 CORELOG-EP (also EP analog of Isothermal $\beta$ model)

The procedure to construct the EP analog of the CORELOG model follows the same procedure as for the NFW model above but starting from the potential given by eqn. (7). We obtain for the potential,

$$\Phi(\tilde{a}) = -\frac{GM_\Delta}{2a_\Delta} \frac{(1+c^2)}{c^2} \ln \left( \frac{1+c^2}{1+(c\tilde{a})^2} \right), \quad (14)$$

where  $c \equiv a_\Delta/a_c$  and  $a_c$  is an ellipsoidal analog of  $r_c$ . The mass and density profiles derived from this potential are respectively,

$$M(< \tilde{a}) = \eta(p_v, q_v) M_\Delta (1+c^2) \frac{\tilde{a}^3}{1+(c\tilde{a})^2}, \quad (15)$$

and,

$$\rho(x, y, z) = \frac{M_\Delta}{4\pi a_\Delta^3} (1+c^2) \frac{1}{(1+(c\tilde{a})^2)^2} \left[ \left( 1 + \frac{1}{p_v^2} + \frac{1}{q_v^2} \right) (1+(c\tilde{a})^2) - \frac{2c^2}{a_\Delta^2} \left( x^2 + \frac{y^2}{p_v^4} + \frac{z^2}{q_v^4} \right) \right]. \quad (16)$$

This expression for the density is the triaxial generalization of the well-known spheroidal form (e.g., Binney & Tremaine 2008).

## 2.4 Ellipsoidal Mass Distributions – EMDs

We define an ellipsoidal mass distribution (EMD) such that the mass density is an ellipsoid of constant shape and orientation; i.e.,  $\rho$  depends only on the ellipsoidal radius  $a_v$ , where now the axial ratios  $p_v$  and  $q_v$  refer to  $\rho$  rather than  $\Phi$ . The gravitational potential generated by an EMD is not an ellipsoid but instead has the form (e.g., Chandrasekhar 1987; Binney & Tremaine 2008),

$$\Phi(\vec{x}) = -\pi G p_v q_v a_\Delta^3 \int_0^\infty \frac{du}{\Delta(u)} \int_{\tilde{a}^2(\vec{x}, u)}^\infty d\tilde{a}'^2 \rho(\tilde{a}'^2), \quad (17)$$

where,

$$\tilde{a}^2(\vec{x}, u) \equiv \frac{x^2}{a_\Delta^2 + u} + \frac{y^2}{(p_v a_\Delta)^2 + u} + \frac{z^2}{(q_v a_\Delta)^2 + u}, \quad \Delta(u) \equiv \sqrt{(a_\Delta^2 + u)((p_v a_\Delta)^2 + u)((q_v a_\Delta)^2 + u)}, \quad (18)$$

and the function  $\Delta(u)$  should not be confused with the over-density value as signified by  $a_\Delta$ . Because the improper integral over  $du$  with upper limit  $\infty$  is inconvenient for numerical evaluation, we follow Merritt & Fridman (1996) and define a new variable,

$$s \equiv \frac{1}{\sqrt{1+u}}, \quad (19)$$

so that,

$$\tilde{a}^2(\vec{x}, s) \equiv s^2 \left[ \frac{x^2}{1+(a_\Delta^2-1)s^2} + \frac{y^2}{1+[(p_v a_\Delta)^2-1]s^2} + \frac{z^2}{1+[(q_v a_\Delta)^2-1]s^2} \right], \quad (20)$$

$$\Delta(s) = \frac{\delta(s)}{s^3}, \quad \delta(s) \equiv \sqrt{(1+(a_\Delta^2-1)s^2)(1+[(p_v a_\Delta)^2-1]s^2)(1+[(q_v a_\Delta)^2-1]s^2)}, \quad (21)$$

$$\Phi(\vec{x}) = -2\pi G p_v q_v a_\Delta^3 \int_0^1 \frac{ds}{\delta(s)} \int_{\tilde{a}^2(\vec{x}, s)}^\infty d\tilde{a}'^2 \rho(\tilde{a}'^2). \quad (22)$$

We use eqn. (22) for all numerical evaluations of EMD potentials in this paper.

### 2.4.1 NFW-EMD

We convert the spherical NFW model to an EMD starting with the mass density defined by eqn. (1) and letting  $r \rightarrow a_v$ ,  $r_\Delta \rightarrow a_\Delta$ , and  $4\pi \rightarrow 4\pi p_v q_v$ ,

$$\rho(\tilde{a}) = \frac{M_\Delta}{4\pi p_v q_v a_\Delta^3} \frac{c^3}{A(c)} \frac{1}{c\tilde{a}(1+c\tilde{a})^2}, \quad (23)$$

where  $c \equiv a_\Delta/a_{\text{scale}}$ , and  $a_{\text{scale}}$  is an ellipsoidal analog of  $r_s$ . From this modified density we compute the mass enclosed within  $a_v$  by direct integration of  $\rho(a_v)$  which gives,

$$M(< \tilde{a}) = M_\Delta \frac{1}{A(c)} \left[ \ln(1+c\tilde{a}) - \frac{c\tilde{a}}{1+c\tilde{a}} \right]. \quad (24)$$

Finally, from the expression for the density we construct the potential,

$$\Phi(\vec{x}) = -\frac{GM_\Delta}{2} \frac{c}{A(c)} \int_0^\infty \frac{du}{\Delta(u)} \frac{1}{1+c\tilde{a}(\vec{x}, u)} = -GM_\Delta \frac{c}{A(c)} \int_0^1 \frac{ds}{\delta(s)} \frac{1}{1+c\tilde{a}(\vec{x}, s)}. \quad (25)$$

For  $p_v = q_v = 1$  this expression for  $\Phi$  reduces exactly to the spherical case (eqn. 3).

### 2.4.2 CORELOG-EMD

The procedure to construct the EMD analog of the spherical CORELOG model is fully analogous to that used for the NFW-EMD model. Converting eqn. (5) to an EMD gives the mass density,

$$\rho(\tilde{a}) = \frac{M_\Delta}{4\pi p_v q_v a_\Delta^3} (1+c^2) \frac{3+(c\tilde{a})^2}{[1+(c\tilde{a})^2]^2}, \quad (26)$$

where  $c \equiv a_\Delta/a_c$ , and  $a_c$  is an ellipsoidal analog of  $r_c$ . From this expression for the density follow the equations for the enclosed mass and the potential as a function of ellipsoidal radius,

$$M(<\tilde{a}) = M_\Delta (1+c^2) \frac{\tilde{a}^3}{1+(c\tilde{a})^2}, \quad (27)$$

and,

$$\Phi(\vec{x}) = -\frac{GM_\Delta}{2} \frac{1+c^2}{c^2} \int_0^\infty \frac{du}{\Delta(u)} \left[ \frac{1}{2} \ln \left( \frac{1+c^2}{1+[c\tilde{a}(\vec{x},u)]^2} \right) + \frac{1}{1+[c\tilde{a}(\vec{x},u)]^2} - \frac{1}{1+c^2} \right], \quad (28)$$

$$= -GM_\Delta \frac{1+c^2}{c^2} \int_0^1 \frac{ds}{\delta(s)} \left[ \frac{1}{2} \ln \left( \frac{1+c^2}{1+[c\tilde{a}(\vec{x},s)]^2} \right) + \frac{1}{1+[c\tilde{a}(\vec{x},s)]^2} - \frac{1}{1+c^2} \right]. \quad (29)$$

Because the integral over  $\tilde{a}$  diverges at  $\infty$ , we replaced the upper limit with  $\tilde{a} = 1$ . With this choice, we have for  $p_v = q_v = 1$  that  $\Phi$  reduces to the spherical case (eqn. 7) but offset by a constant so that,  $\Phi(r_\Delta) = -GM_\Delta/r_\Delta$ , rather than  $\Phi(r_\Delta) = 0$ .

## 3 FIDUCIAL MASS MODEL PARAMETERS AND AXIAL RATIO PROFILES

The ellipsoidal NFW and CORELOG models have four free parameters that need to be specified: concentration ( $c$ ), mass ( $M_\Delta$ ), and axis ratios ( $p_v, q_v$ ). The axis ratios refer to the potential for an EP and to the mass distribution for an EMD. As we show below in §5, our results are not very sensitive to the degree of triaxiality of the ellipsoid as quantified by the triaxiality parameter  $T$  (Franx et al. 1991). Consequently, unless stated otherwise, throughout this paper we set,

$$p_v = \sqrt{1 - T(1 - q_v^2)} = \sqrt{\frac{1 + q_v^2}{2}}, \quad (30)$$

where we adopt  $T = 0.5$  for the ‘‘maximally triaxial’’ ellipsoid that lies midway between the oblate ( $T = 0$ ) and prolate ( $T = 1$ ) spheroids.

Since we also find that our results are very insensitive to the halo mass scale over the range of interest ( $10^{12} - 10^{15} M_\odot$ ), we adopt a fiducial mass,  $M_\Delta = 10^{14} M_\odot$ , which lies near the middle of this range. With this value for the mass, we set the NFW concentration to  $c = 9$  (assuming  $\Delta \approx 100$ ) appropriate for the results we obtained from X-ray measurements spanning the same large mass range (Buote et al. 2007). Although this normalization of the concentration-mass relation is 30-60% larger than that obtained from dissipationless cosmological simulations (e.g., Macciò et al. 2008), the results we present in this paper are unchanged if instead we use such a smaller concentration value. These values for  $c$  and  $M_\Delta$  are used for both the EP and EMD variations of the NFW model. To provide a clear contrast with the NFW models, we adopt a large value of the concentration parameter ( $c = 100$ ) for all CORELOG models which insures nearly scale-free behavior (e.g,  $M \sim a_v$  for EP) over most of the system.

Using these fiducial parameters for the EP models, we display in Figure 1 the (short-to-long) axial ratios  $q_\rho$  of the isodensity contours plotted as a function of  $a_v/a_\Delta$  (with  $\Delta = 100$ ) for different values of  $q_\Phi \equiv q_v$ , the axial ratio of the potential ellipsoid. We consider the range,  $q_\Phi = 0.7 - 1$ , corresponding to approximately,  $q_\rho = 0.4 - 1$ , appropriate for  $\Lambda$ CDM halos (e.g., Bailin & Steinmetz 2005, and references therein). The  $q_\rho$  were computed for a given  $a_v$  by solving the equation,  $\rho(a_v, 0, 0) = \rho(0, 0, z)$ , for  $z$  and then setting  $q_\rho = z/a_v$ . We find that for both models, as is typical for EPs, that  $q_\rho$  decreases (i.e., the density distribution becomes flatter) with increasing  $a_v$ . As  $a_v$  approaches  $a_\Delta$ ,  $q_\rho$  approaches a constant value for each  $q_\Phi$  for CORELOG-EP, whereas  $q_\rho$  continues to decrease for NFW-EP; i.e., the NFW-EP mass distribution is flatter than CORELOG-EP for  $a_v \sim a_\Delta$  and is slightly rounder for  $a_v \sim 0.01 a_\Delta$ . (Note that for  $q_\Phi < 0.8$  the density of the fiducial NFW-EP model takes negative values on the  $z$  axis for some  $z < a_\Delta$ .) We mention that the decrease of  $q_\rho$  with radius for the NFW-EP model disagrees with the generally increasing trend found in dissipationless cosmological simulations (e.g., Bailin & Steinmetz 2005; Allgood et al. 2006), although  $q_\rho$  profiles that decrease with radius tend to result when dissipation is considered (e.g., Kazantzidis et al. 2004; Debattista et al. 2008).

For EMD models with the fiducial parameters, we display in Figure 2 the axial ratios ( $q_\Phi$ ) of the isopotential contours plotted as a function of  $a_v/a_\Delta$  for different values of  $q_\rho \equiv q_v$ , the axial ratio of the mass (density) ellipsoid. The  $q_\Phi$  were computed for a given  $a_v$  by solving the equation,  $\Phi(a_v, 0, 0) = \Phi(0, 0, z)$ , for  $z$  and then setting  $q_\Phi = z/a_v$ . For both the NFW-EMD and CORELOG-EMD models  $q_\Phi$  increases (i.e., the potential becomes rounder) with increasing radius, though

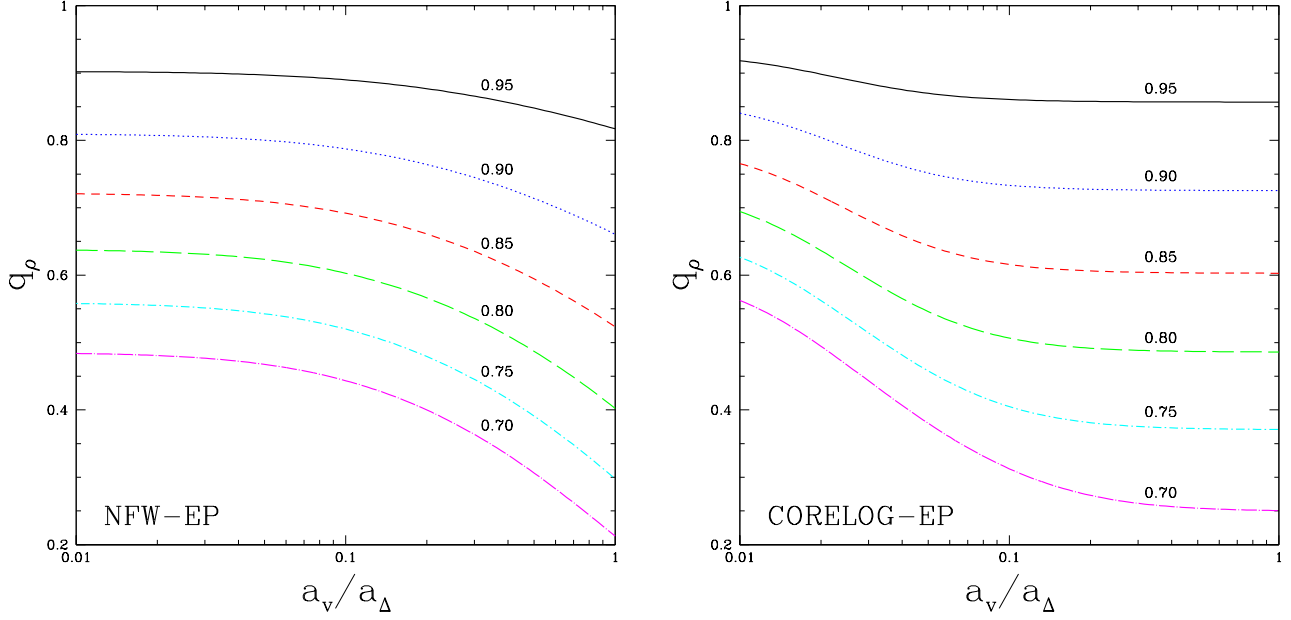


**Figure 1.** Axial ratio profiles of the mass density for the fiducial NFW-EP (*Left Panel*) and CORELOG-EP (*Right Panel*) models (§3). Shown are results for six values of the axial ratio in the potential  $q_\Phi$ . Note that for hydrostatic equilibrium the axial ratio of the X-ray emissivity is the same as the potential, independent of the temperature profile (see §4.1).

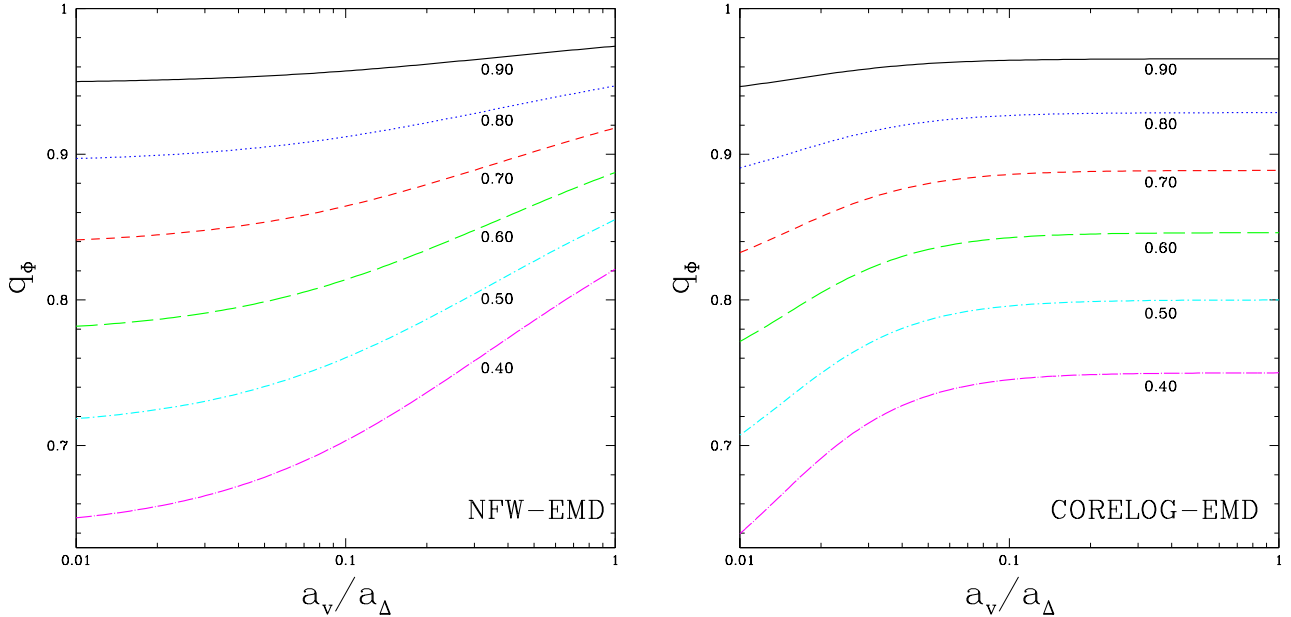


**Figure 2.** Axial ratio profiles of the potential for the fiducial NFW-EMD (*Left Panel*) and CORELOG-EMD (*Right Panel*) models (§3). Shown are results for six values of the axial ratio in the mass density  $q_\rho$ . Note that for hydrostatic equilibrium the axial ratio of the X-ray emissivity is the same as the potential, independent of the temperature profile (see §4.1).

for CORELOG-EMD  $q_\Phi$  attains a constant value for  $a_v \gtrsim 0.1a_\Delta$  for all  $q_\rho$  explored. Generally, for  $a_v \sim a_\Delta$  the potential is rounder for NFW-EMD compared to a CORELOG-EMD model with the same  $q_\rho$ . The models have very similar values of  $q_\Phi$  for  $a_v \sim 0.01a_\Delta$ .



## 4 METHOD TO TEST SPHERICAL AVERAGING

Our objective is to quantify average biases and scatter in cluster properties arising from inconsistent spherical averaging procedures employed by observers and theorists, with particular attention devoted to properties measured by X-ray and SZ studies. It is most common for the theorist to spherically average the three-dimensional cluster available in their models, from which “true” spherically averaged quantities are derived. The observer, however, has access only to the cluster projected onto the sky. Generally, the observer circularly averages the cluster data projected onto the sky and then performs a deprojection assuming spherical symmetry. We refer to cluster properties inferred from such a deprojection as “observed” spherically averaged properties. By comparing the “observed” and “true” values for clusters of different shapes and projection orientations we quantify any bias due to spherical averaging in this way. Below we provide more details on how we make this comparison.

### 4.1 Hydrostatic Equilibrium – Gas Mass and X-ray Emissivity

To associate X-ray emission with a cluster entails filling the gravitational potential well with hot plasma, which is approximated very well by a non-rotating ideal gas in hydrostatic equilibrium,

$$\nabla P_{\text{gas}} = -\rho_{\text{gas}} \nabla \Phi, \quad (31)$$

where  $P_{\text{gas}}$  is the thermal pressure and  $\rho_{\text{gas}}$  is the gas density. For an isothermal gas, this equation can be solved for the gas density to yield,

$$\rho_{\text{gas}}(\vec{x}) = \rho_{\text{gas},0} \exp\left(\frac{\mu m_a}{k_B T} [\Phi_0 - \Phi(\vec{x})]\right), \quad (32)$$

where  $\rho_{\text{gas},0}$  and  $\Phi_0$  are, respectively, the central values of the gas density and the potential, and  $T$  is the (constant) temperature of the gas. Our study focuses on the isothermal solution because temperature gradients have little impact on the flattening of X-ray images of galaxies and clusters. This is a consequence of the isopotential surfaces having the same shapes as the constant surfaces of gas density, temperature, and X-ray emissivity; i.e., the X-ray Shape Theorem (Buote & Canizares 1994, 1996a; Buote & Humphrey 2012). In fact, in Theorem 7 of Paper 1 we show that the observed deprojected spherically averaged mass profile for any EP model is independent of the temperature profile. Nevertheless, because other quantities may be more affected, we also explore models with temperature gradients using a polytropic equation of state  $P_{\text{gas}} \propto \rho_{\text{gas}}^\gamma$ . Inserting this relationship between the pressure and density into eqn. (31) gives (e.g., Sarazin 1986),

$$T(\vec{x}) = T_0 + \frac{\gamma - 1}{\gamma} \frac{\mu m_a}{k_B} (\Phi_0 - \Phi(\vec{x})), \quad (33)$$

$$\rho_{\text{gas}}(\vec{x}) = \rho_{\text{gas},0} \left(\frac{T(\vec{x})}{T_0}\right)^{\frac{1}{\gamma-1}}. \quad (34)$$

We focus our attention on models with  $\gamma = 1.2$  which best represent the falling temperature profiles (outside of any cool core) of observed clusters and those produced in cosmological simulations (e.g., Ostriker et al. 2005).

To define completely these models we need to specify the normalizations of the temperature and density profiles of the hot gas. We normalize the temperature using the  $M_{500} - T_X$  relation given by Arnaud et al. (2005, 2007). For isothermal models, we simply set  $T = T_X$ . For the polytropic models we determine the normalization constant  $T_0$  by computing the gas-mass-weighted temperature within a radius of  $r_{500}$  and then set the result equal to  $T_X$ . The results presented below in §5 are very insensitive to the adopted form of the  $M_{500} - T_X$  relation.

Similarly, we normalize the gas density using the  $M_{500} - M_{\text{gas},500}$  relation given by Arnaud et al. (2007). That is, we determine  $\rho_{\text{gas},0}$  by computing the total gas mass within a radius of  $r_{500}$  and then set it equal to  $M_{\text{gas},500}$ . While this normalization is convenient, it is not strictly necessary because we choose to neglect the self-gravity of the gas in our models ( $\Phi_{\text{gas}} \ll \Phi$ ) – see beginning of §2.

Given the gas density and temperature we compute the X-ray emissivity,  $\epsilon_X = \rho_{\text{gas}}^2 \Lambda(T)$ , where  $\Lambda(T)$  is the plasma emissivity for a coronal plasma, which we take to be the APEC model (Smith et al. 2001) as implemented in XSPEC (Arnaud 1996) integrated over energies 0.5–8 keV. We assume a constant metallicity of 0.5 solar throughout the system, though our analysis is not very sensitive to the assumed abundance profile. For isothermal models, we set  $\Lambda = 1$  so that the emissivity is simply,  $\epsilon_X = \rho_{\text{gas}}^2$ .

### 4.2 True Spherically Averaged Profiles of Mass and other Quantities

For a given mass model (§2) we compute the true spherically averaged profile of the (total) mass as follows. For EP models the spherical averaging of the mass profile is conveniently achieved by applying Gauss’s Law over a sphere of radius  $r$  (Theorem 2 of Paper 1). There is no such simplification for the EMD models, where instead we directly integrate the density (i.e., either eqn. 23 or 26) over a spherical volume. We evaluate the spherically averaged mass profile in 500 (200) logarithmically spaced

bins for EP (EMD) models within a radius  $r = a_\Delta$ , where  $\Delta = 100$  (§3). By fitting this profile with the spherical version of the mass model (e.g., NFW – eqn. 2), we obtain the “true” spherically averaged parameters for the mass model,  $c_{\text{sp}}$  and  $M_{\Delta, \text{sp}}$ . For consistency with the observed mass analysis (see §4.5), the fitting is performed only within  $r = (p_v q_v)^{1/3} a_{500}$  which is  $\approx r_{500}$ . Note in most cases at least 80% of the logarithmically spaced bins are within this radius. Moreover, the inferred values of  $c_{\text{sp}}$  and  $M_{\Delta, \text{sp}}$  are not very sensitive to small changes ( $\sim 10\%$ ) in the outer radius used in the fits.

Having chosen both a mass model and a gas equation of state (§4.1) we compute the spherically averaged profiles of quantities directly associated with the hot gas. For EMD models we compute the “true” spherically averaged gas mass ( $M_{\text{gas,sp}}$ ) by integrating  $\rho_{\text{gas}}$  over a spherical volume of radius  $r = r_{500}$ , where  $r_{500}$  is evaluated using  $M_{500, \text{sp}}$  determined by fitting the mass profile as described above. For EPs the effective spherical average is used by setting  $M_{\text{gas,sp}} = M_{\text{gas}}(< (p_v q_v)^{-1/3} r_{500})$ , which is the three-dimensional analog of Definition 1 of Paper 1. These procedures insure a consistent comparison of the gas mass with the observations (§4.5). It then follows that the spherically averaged gas fraction is,  $f_{\text{gas,sp}} = M_{\text{gas,sp}}/M_{500, \text{sp}}$ . For the emission weighted temperature ( $T_{X, \text{sp}}$ ) we integrate  $\epsilon_X T$  within  $r_{500}$  and then divide by the luminosity within that volume. Using the temperature and gas mass we compute,  $Y_{X, \text{sp}} = M_{\text{gas,sp}} T_{X, \text{sp}}$  (Kravtsov et al. 2006). Finally, since the integrated Compton-y parameter is proportional to the volume integral of the gas pressure (e.g., eqn. 48 of Paper 1), we set  $Y_{\text{SZ,sp}}$  equal to the integral of  $P_{\text{gas}}$  within  $r_{500}$ , ignoring proportionality constants which are unimportant for our study.

### 4.3 Projection

We construct the X-ray image by projecting the X-ray emissivity onto the sky for a given orientation. In Paper 1 we present analytical formulas for EPs relating the “observed” deprojected spherically averaged quantities (e.g., mass, gas mass, etc.) to their three-dimensional ellipsoidal counterparts. This means that for a given shape and projection orientation one may, e.g., immediately evaluate the “observed” deprojected spherically averaged mass profile for NFW-EP using eqn. (12) inserted into the result of Theorem 7 of Paper 1. Nevertheless, in our present investigation we find it useful to carry out the projection (and subsequent deprojection) numerically in order to test the accuracy of other aspects of our computer code, particularly via comparison to the EMDs which cannot be evaluated with simple analytical formulas.

Since the X-ray emissivity of an EP is an ellipsoid, we follow the procedure described in § 5 of Paper 1 and carry out the projection by partitioning the emissivity into a series of concentric, similar triaxial ellipsoidal shells and by approximating the emissivity as a constant within each shell. For such a system viewed with orientation  $(\theta, \phi)$ , expressions for the surface brightness  $\Sigma_{X,i}$  and temperature map  $\langle T \rangle_i$  are given by eqns. (66) and (69) in Paper 1. Each quantity is defined within an elliptical annulus  $i$  on the sky with inner semi-major axis  $\alpha_{i-1}$ , outer semi-major axis  $\alpha_i$ , and axial ratio  $q_s$  (eqn. 18 of Paper 1) which is same for all annuli.

We compute the surface brightness of an EMD,  $\Sigma_X(x', y') = \int \epsilon_X(\vec{x}') dz'$ , via full integration of the X-ray emissivity along the line-of-sight for a given  $(\theta, \phi)$ . Using the same procedure we compute the emission-weighted temperature map,  $\langle T \rangle(x', y') = \int \epsilon_X(\vec{x}') T(\vec{x}') dz' / \Sigma_X(x', y')$ . The integrations proceed interior to the isopotential surface that passes through  $a_\Delta$  on the major axis. Since the potential of an EMD is not itself ellipsoidal in shape, but is very nearly so, we approximate this boundary surface by an ellipsoid in our computations.

We make no further modifications to the model surface brightness and temperature map. In particular, we do not fold the image through an image point spread function, nor do we fold the spectrum through a response matrix. We assume the observer is able to account for such issues perfectly, so our analysis is able to focus on potential biases arising only from geometrical issues associated with projection and spherical averaging of the galaxy or cluster.

(Note that the sky map of the Compton-y parameter is obtained in the same manner as  $\Sigma_X$  by replacing the emissivity with the gas pressure.)

### 4.4 Spherical Deprojection

Now turning our perspective to that of an observer, we begin with the surface brightness, temperature, and Compton-y maps on the sky as produced in the previous section. In general these maps have non-circular shapes, but it is the goal of the fictitious observer to infer spherically averaged profiles from these maps. To this end we follow standard practice and bin the surface brightness into a series of  $N$  concentric, circular annuli defined so that  $R_i$  is the outer radius of annulus  $i$ . For consistency, we use the same bin definitions adopted in §4.2 for the three-dimensional radius of the true mass profile; i.e., we associate each  $R_i$  on the sky with the equivalent  $r_i$  in three dimensions defined in §4.2.

The procedure to create the circular binning differs for the EP and EMD models. For EPs the constructed image is already binned in elliptical annuli, where the annuli definitions correspond to elliptical versions of the spherical radii adopted in §4.2 for the true mass profile; i.e., for each bin we have  $\alpha_i = a_{v,i} = r_i$ , where  $\alpha_i$  is the outer semi-major axis of elliptical annulus  $i$  on the sky and  $a_{v,i}$  is the outer semi-major axis of the shell  $i$  in three dimensions. To achieve the circular binning on the sky, for  $\Sigma_{X,i}$  defined in each elliptical bin we associate an inner radius  $R_{i-1} \equiv \alpha_{i-1} \sqrt{q_s}$  and an outer radius  $R_i \equiv \alpha_i \sqrt{q_s}$  (see Definition 1 of Paper 1). In contrast, for the circular binning of the EMDs we must resort to computing,  $\int \Sigma_X(x', y') dx' dy'$ , the

full integration of the surface brightness over each circular bin ( $R_{i-1}, R_i$ ), a much more computationally expensive procedure than for the EPs. To improve computational speed for the EMDs we use only ten points, equally spaced in azimuth, for each circular bin. We also take advantage of the elliptical symmetry and perform the calculation over half of the circle. Finally, as in previous studies (e.g., Lewis et al. 2003, see also McLaughlin 1999), we find it useful for each annulus to choose an intermediate average radius to represent the result for the entire bin.

We obtain the observed radial volume emissivity in each shell  $i$  ( $\epsilon_i^{\text{sp,obs}}$ ) by deprojecting the circularly averaged surface brightness ( $\Sigma_{X,i}^{\text{circ}}$ ) using the standard spherical ‘‘onion peeling’’ method (Fabian et al. 1981; Kriss et al. 1983). In particular, we convert the binned surface brightness values into luminosities,  $L_i^{\text{circ}} = \pi(R_i^2 - R_{i-1}^2)\Sigma_{X,i}^{\text{circ}}$  and then apply the onion peeling method as given by eqn. (66) of Paper 1 but using the spherical version of the projection matrix  $V_{ij}^{\text{int}}$ . This procedure is also used for the SZ map where the pressure takes the place of the emissivity, and  $L_i^{\text{circ}}$  is replaced by the Compton- $y$  parameter within bin  $i$ .

The observed spherically averaged gas density follows immediately from the emissivity,  $\rho_{\text{gas},i}^{\text{sp,obs}} = \sqrt{\epsilon_i^{\text{sp,obs}}}$ , for isothermal models. For the models with temperature gradients, however, we require the temperature profile in order to evaluate the density. To deproject the temperature map we follow the same procedure as for the surface brightness with the following substitutions to eqn. (66) of Paper 1:  $L_i \rightarrow \langle T \rangle_i L_i$  and  $\epsilon \rightarrow \epsilon T$ . The result is the radial profile of the product of the emissivity and the temperature ( $\epsilon T$ ) $_i^{\text{sp,obs}}$  in three dimensions. Using this, along with the deprojected emissivity, gives the radial temperature profile,  $T_i^{\text{sp,obs}} = (\epsilon T)_i^{\text{sp,obs}} / \epsilon_i^{\text{sp,obs}}$ , which allows the gas density to be computed,  $\rho_{\text{gas},i}^{\text{sp,obs}} = \sqrt{\epsilon_i^{\text{sp,obs}} / \Lambda(T_i^{\text{sp,obs}})}$ . (We assume the observer has perfect knowledge of the constant metallicity for evaluation of  $\Lambda$ .)

#### 4.5 Observed Spherically Averaged Mass Profile

From the observed spherically averaged density and temperature profiles, we compute the mass profile assuming hydrostatic equilibrium,

$$M(< r)_{\text{sp}}^{\text{obs}} = - \left[ \frac{r k_B T_{\text{sp}}^{\text{obs}}}{\mu m_a G} \right] \left[ \frac{d \ln \rho_{\text{gas,sp}}^{\text{obs}}}{d \ln r} + \frac{d \ln T_{\text{sp}}^{\text{obs}}}{d \ln r} \right], \quad (35)$$

where we evaluate the derivatives by interpolating the binned profiles with cubic splines (except for the outermost bin where we use logarithmic interpolation). We compute the mass profile in the same radial bins as done for the true mass profile (§4.2), and then fit this observed mass profile with the same spherical version of the mass model to obtain the observed spherically averaged model parameters,  $c_{\text{sp}}^{\text{obs}}$  and  $M_{\Delta,\text{sp}}^{\text{obs}}$ . In order to minimize any weak sensitivity of our results to the chosen outer boundary defined by the elliptical radius  $a_{100}$  in the potential (mass) for EPs (EMDs), we performed the fitting of the observed mass profile within a smaller radius. As remarked already in §4.2, we adopted  $r_{500}$  for this purpose, although we found little difference when using other conventional choices (e.g.,  $r_{2500}, r_{200}$ ). The procedure to determine the other gas parameters is the same as described for the ‘‘true’’ values in §4.2. For example, for both EP and EMD models we compute the spherically averaged gas mass ( $M_{\text{gas,sp}}^{\text{obs}}$ ) by integrating  $\rho_{\text{gas,sp}}^{\text{obs}}$  within a spherical volume of radius  $r = r_{500}$ , where  $r_{500}$  is evaluated using  $M_{500,\text{sp}}^{\text{obs}}$ , from which immediately follows the spherically averaged gas fraction,  $f_{\text{gas,sp}}^{\text{obs}} = M_{\text{gas,sp}}^{\text{obs}} / M_{500,\text{sp}}^{\text{obs}}$ . In the same way we compute  $Y_{\text{SZ,sp}}^{\text{obs}}$  within  $r_{500}$ , though we note that in practice SZ observations without corresponding X-ray data must estimate  $r_{500}$  in a different manner.

## 5 RESULTS

### 5.1 Preliminaries

For our comparison of the ‘‘observed’’ (§4.5) with the ‘‘true’’ (§4.2) spherically averaged quantities, we will focus on the percentage bias for each parameter; e.g., the total mass,

$$100\% \left( \frac{M - M_{\text{true}}}{M_{\text{true}}} \right) \equiv 100\% \left( \frac{M_{500,\text{sp}}^{\text{obs}} - M_{500,\text{sp}}^{\text{true}}}{M_{500,\text{sp}}^{\text{true}}} \right), \quad (36)$$

where we suppress the notation for the spherical averaging, over-density, and ‘‘obs’’ denoting the observed quantity. With regard to the numerical accuracy of the biases presented below, there are differences between the EP and EMD models. In Paper 1 we showed that for EPs the deprojected spherical average of a parameter (e.g.,  $M_{500,\text{sp}}^{\text{obs}}$ )<sup>1</sup> can be evaluated directly from the ellipsoidal distribution (e.g.,  $M(< a_v)$ ) without the need to perform explicitly any projection and deprojection. Consequently, the biases for EPs can be evaluated extremely accurately and efficiently. Recall in §4.3 we chose, nevertheless, to numerically project and deproject the EPs to assess the performance of our computer code. We found no significant

<sup>1</sup> For an EP this is also denoted by  $\langle M(< r_{500}) \rangle^{\text{d+}}$  using the notation of Paper 1.

**Table 1.** Polynomial Approximations of the Average Biases as a Function of  $q_v$ 

Bias or $\sigma$	NFW-EP				NFW-EMD			
	$c_0$	$c_1$	$c_2$	$c_3$	$c_0$	$c_1$	$c_2$	$c_3$
Concentration	-42.93	114.87	-101.68	29.74	-9.32	24.93	-23.45	7.87
$\sigma$	21.82	-37.60	20.81	-5.04	14.64	-32.60	27.54	-9.60
Mass	17.95	-45.95	38.18	-10.18	5.60	-15.26	14.53	-4.89
$\sigma$	6.58	-10.47	5.28	-1.39	6.38	-14.94	13.27	-4.71
Gas Mass	6.29	-14.34	9.96	-1.91	1.12	0.83	-3.80	1.85
$\sigma$	-10.52	33.89	-32.09	8.72	1.70	0.45	-3.96	1.82
Gas Fraction	-11.07	29.86	-26.52	7.73	-4.25	15.24	-17.27	6.31
$\sigma$	16.03	-40.87	33.56	-8.72	4.29	-11.68	11.17	-3.79
$Y_{SZ}$	-7.67	19.97	-17.58	5.30	-1.74	8.67	-10.80	3.95
$\sigma$	50.80	-108.78	79.78	-21.80	7.97	-15.47	10.75	-3.26
$Y_{SZ,X}$	-15.49	40.19	-34.84	10.14	-2.63	7.28	-6.58	2.00
$\sigma$	39.08	-71.35	44.20	-11.93	9.46	-14.65	6.47	-1.28

The orientation-angle-average bias and standard deviation as a function of  $q_v$  approximated by a cubic polynomial:  $c_0 + c_1q_v + c_2q_v^2 + c_3q_v^3$ . Results are given for the triaxial, isothermal NFW models evaluated at  $r_{500}$ ; c.f. Figures 4, 5, 8, 10.

differences between the results obtained via numerical projection and deprojection with those obtained using the analytical formulas from Paper 1; i.e., the numerical uncertainty for the EPs is negligible for our investigation.

However, the much higher computational expense of the EMD models, owing to the need for numerical integration of their non-analytical potentials, limits the number of radial and azimuthal grid points that can be practically employed, rendering the EMDs less accurate than the EPs. By experimenting with models having different numbers of radial and azimuthal grid points and having different tolerance precisions for the numerical integrations, we conclude that in most cases the numerical uncertainty of the EMDs is negligible for our investigation. The largest uncertainties usually occur for models with the smallest axial ratios ( $q_v < 0.5$ ) which translate at most to bias errors of  $\approx 0.2\%$  for EMDs.

## 5.2 Bias Distributions

We construct bias probability distributions by evaluating eqn. (36) (appropriate for each parameter) for a large number of viewing orientations  $(\theta, \phi)$  generated by randomly sampling the solid angle over the orientation sphere. By taking advantage of the ellipsoidal symmetry of the cluster models, we restrict the orientation angles to the first octant of the sphere; i.e.,  $0 \leq \cos \theta \leq 1$  and  $0 \leq \phi \leq \pi/2$ . In Figure 3 we display the bias distributions generated by  $10^4$  random orientations of the isothermal NFW-EP model with  $q_v = 0.70$  for the gravitational potential. All of the distributions are non-gaussian and somewhat asymmetric, though they are peaked toward the center. Interestingly, the mean bias for each parameter is significantly different from zero; i.e., biases are not eliminated through angle-averaging. As  $q_v$  increases toward 1 the distributions of the isothermal NFW-EP model become progressively narrower and more symmetric (not shown). Despite the non-gaussian behavior for smaller  $q_v$ , the mean and standard deviation provide a useful, convenient characterization of each distribution, which we employ below to frame our discussion of the systematic variations of the bias distributions with  $q_v$ .

## 5.3 Angle Averages and Standard Deviations

In Figures 4, 5, 8, 10, 12, and 13 we plot the mean and standard deviations of the bias distributions versus  $q_v$  for the concentration, mass, gas mass, gas fraction,  $Y_{SZ}$  and  $Y_{SZ,X}$  computed within  $r_{500}$  for the isothermal models as well as the polytropic EMD models. The results for EP models reflect 500 random orientations while the more computationally expensive EMD models reflect 200 random trials. For comparison, for the case of the isothermal EPs we also display results for models computed within  $r_{2500}$  (Figure 14) and for spheroidal NFW-EP models (Figure 15). Results for  $T_X$  and  $Y_X$  using polytropic models are displayed in Figure 11. All the figures plot the biases over the same range to facilitate visual comparison. Finally, in Table 1 we provide analytical approximations to the mean bias and standard deviation profiles for the triaxial isothermal NFW models computed within  $r_{500}$ , which we find are represented very well by cubic polynomials.

### 5.3.1 Concentration

The concentration parameter displays the largest mean bias magnitude of the parameters investigated. While still not large in absolute terms, as seen in Figure 4 the average bias is nearly -2% for the smallest axial ratios considered. In addition, next to  $Y_{SZ}$  (§5.3.7) the concentration possesses the largest scatter. The NFW and CORELOG models have nearly identical average

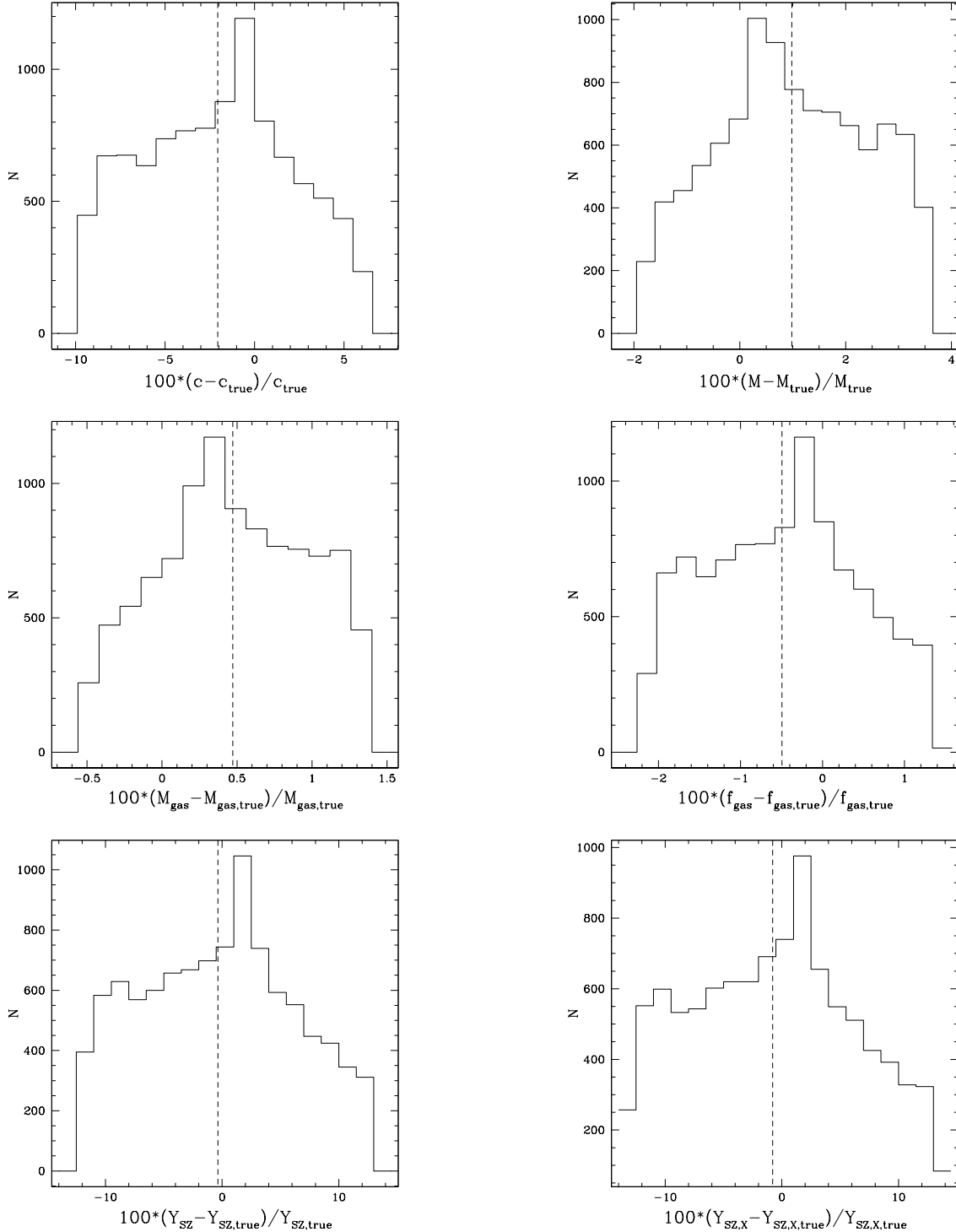


**Figure 3.** Bias distributions generated from  $10^4$  random trials in viewing orientation for the isothermal NFW-EP models with  $q_v = 0.70$  for the gravitational potential. Displayed are results for the concentration (*top, left*), mass (*top, right*), gas mass (*middle, left*), gas fraction (*middle, right*),  $Y_{SZ}$  (*bottom, left*), and  $Y_{SZ,X}$  (*bottom, right*). The vertical dashed lines show the mean of each distribution.

biases, though CORELOG has a slightly larger scatter. Since the deprojected spherically averaged mass profile of an EP is independent of the temperature profile (Theorem 7 of Paper 1), temperature gradients do not affect the bias distribution for the concentration of an EP. Comparing the isothermal and polytropic EMD models in Figure 4, one sees that the EMDs are only a little affected by having different temperature profiles; i.e., the polytropic EMDs have slightly larger scatter and slightly smaller average bias magnitudes. The concentration biases are essentially the same when the results are computed within the smaller aperture  $r_{2500}$  (Fig. 14) or when spheroids are adopted instead of the default maximally triaxial ellipsoid

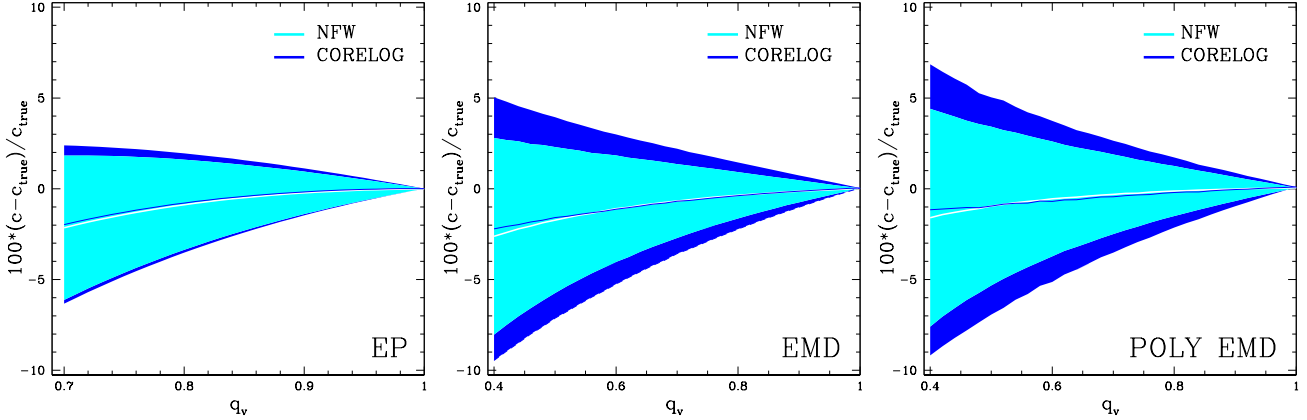


**Figure 4.** Bias on the concentration parameter as a consequence of spherical averaging. (*Left Panel*) Results are shown for isothermal EP models plotted as a function of  $q_v$  in the gravitational potential. (In hydrostatic equilibrium this is also the  $q_v$  of the X-ray emissivity.) The solid lines are orientation angle-averaged values (NFW – white, CORELOG – blue), while the shaded regions (NFW – light blue/cyan, CORELOG – dark blue) are the  $1\sigma$  ranges. (*Middle Panel*) Same as the left panel except now the EMD models are shown and, therefore,  $q_v$  corresponds to the axial ratio of the mass density profile. (*Right Panel*) Same as the middle panel except now results for the  $\gamma = 1.2$  polytrope with a temperature gradient are shown.

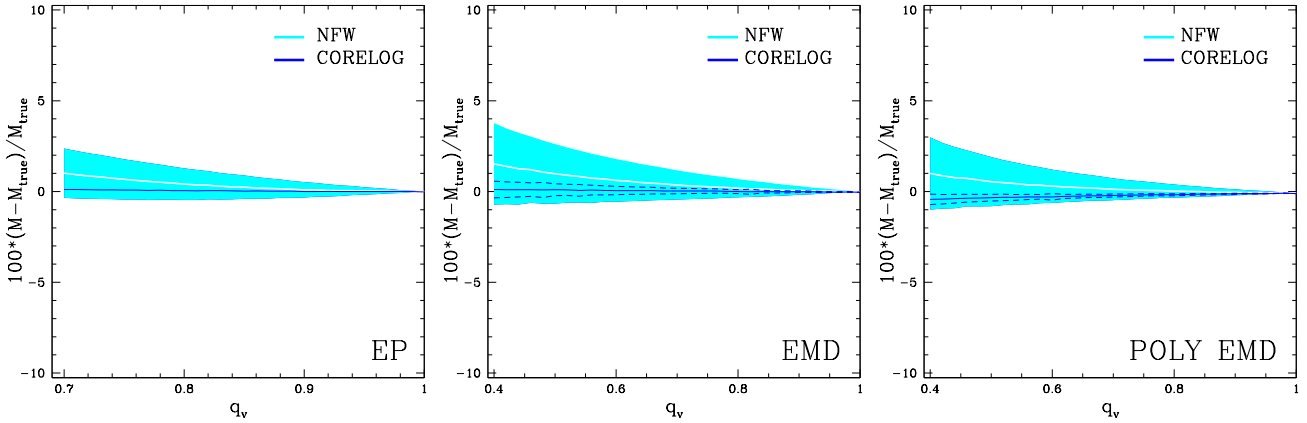


**Figure 5.** Same as Figure 4 except now the bias on the mass is shown. For clarity, the blue dashed lines also represent the  $1\sigma$  CORELOG region when it is contained within the  $1\sigma$  NFW region. Note that the  $1\sigma$  region for CORELOG-EP is negligible.

(Fig. 15). Perhaps the most notable difference is the slightly more negative average bias for the oblate NFW spheroids. Note also that because our implementation of the CORELOG model with a large concentration results in essentially a scale-free model, all the CORELOG parameter biases (including the concentration) are essentially unchanged when computed within  $r_{2500}$  compared to the default  $r_{500}$ .

Overall, the concentration parameter biases exhibit some general behavior that apply to most of the other parameters. These trends are usefully described with respect to the projections down each of the three principal axes, which we summarize here. Of the three principal axes, the smallest mean bias magnitude occurs for the intermediate-axis projection, while the projections along the short and long axes bracket the full range of biases for all orientations. The short-axis projection underestimates the true value, and the long-axis projection overestimates it. For the specific case of the concentration parameter, these trends can be explained because the concentration is defined to be inversely proportional to the scale radius of the mass profile. It is reasonable to expect that the scale radius tends to be overestimated when the ellipsoid is projected along the short axis because the two longest axes then lie in the sky plane. Conversely, the scale radius tends to be underestimated when the ellipsoid is projected down the long axis because then the two shortest axes lie in the sky plane.

### 5.3.2 Mass

The NFW and CORELOG models exhibit interesting differences in their mass biases. The average bias of the NFW models is small but significant, increasing to  $\sim 1\%$  for the smallest axial ratios (Fig. 5). The  $1\sigma$  scatter for NFW models is similarly

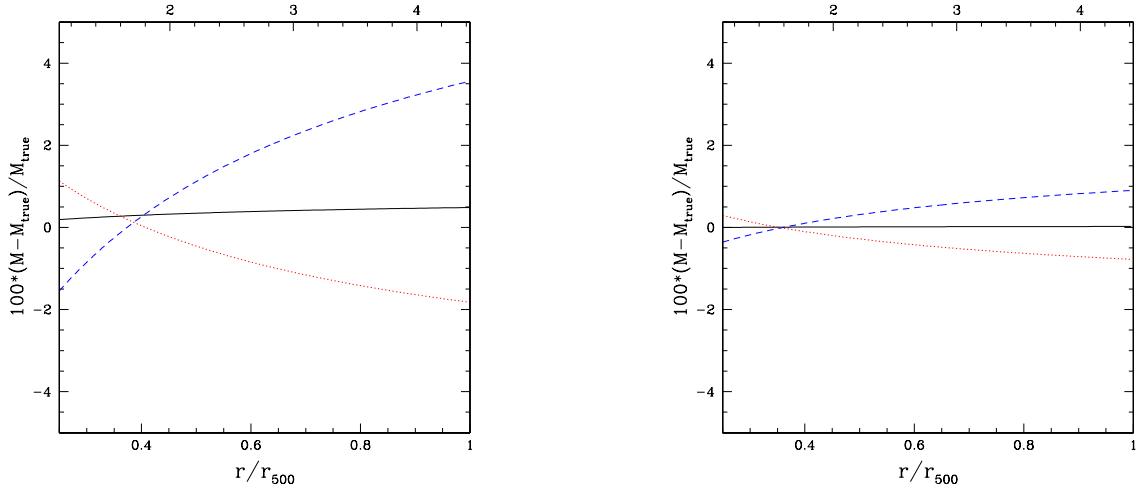


**Figure 6.** Bias of the mass plotted as a function of radius between  $0.25 - 1r_{500}$  for the isothermal NFW-EP model for  $q_v = 0.7$  (left panel) and  $q_v = 0.9$  (right panel) in the gravitational potential. Results are displayed for projections down the three principal axes: short (dashed, blue), long (dotted, red), and intermediate (solid, black). The top axis gives  $r/r_s$ , where  $r_s$  is the NFW-EP scale radius.

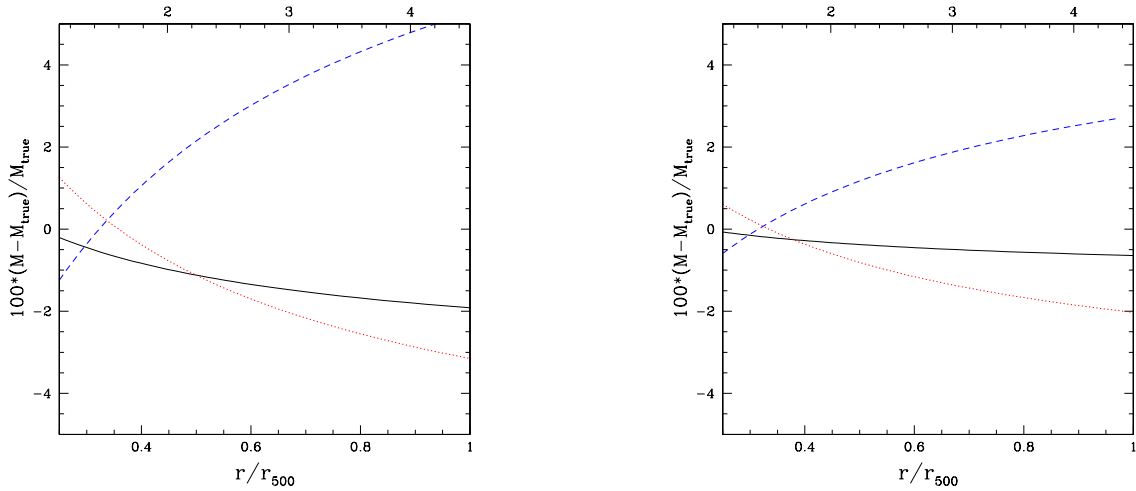


**Figure 7.** Bias of the mass plotted as a function of radius between  $0.25 - 1r_{500}$  for the isothermal NFW-EMD model for  $q_v = 0.4$  (left panel) and  $q_v = 0.6$  (right panel) in the mass. Results are displayed for projections down the three principal axes: short (dashed, blue), long (dotted, red), and intermediate (solid, black). The top axis gives  $r/r_s$ , where  $r_s$  is the NFW-EMD scale radius.

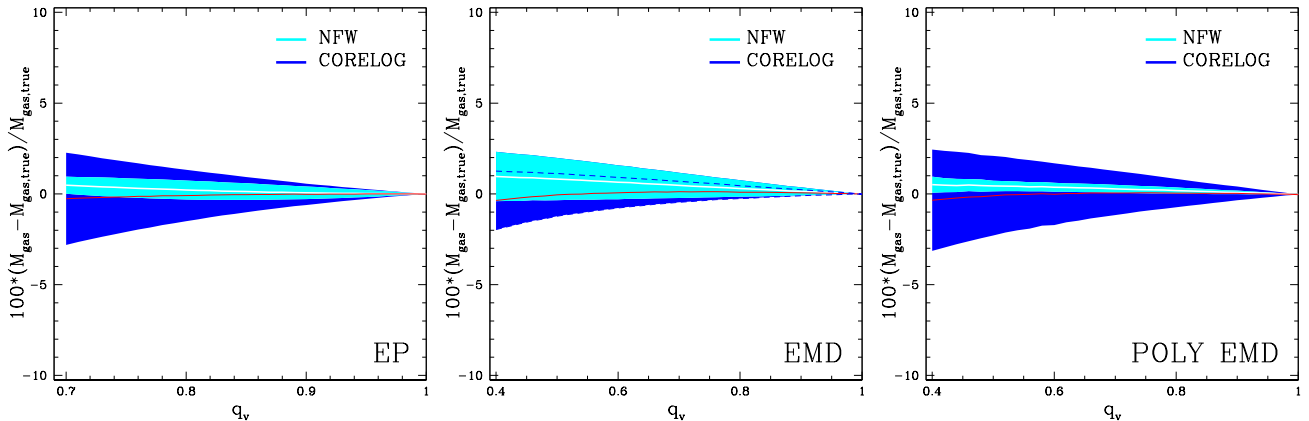


**Figure 8.** Same as Figure 4 except now the bias on the gas mass is shown. For clarity, the blue dashed lines also represent the  $1\sigma$  CORELOG region when it is contained within the  $1\sigma$  NFW region, and the average bias for CORELOG is denoted by the red solid line.

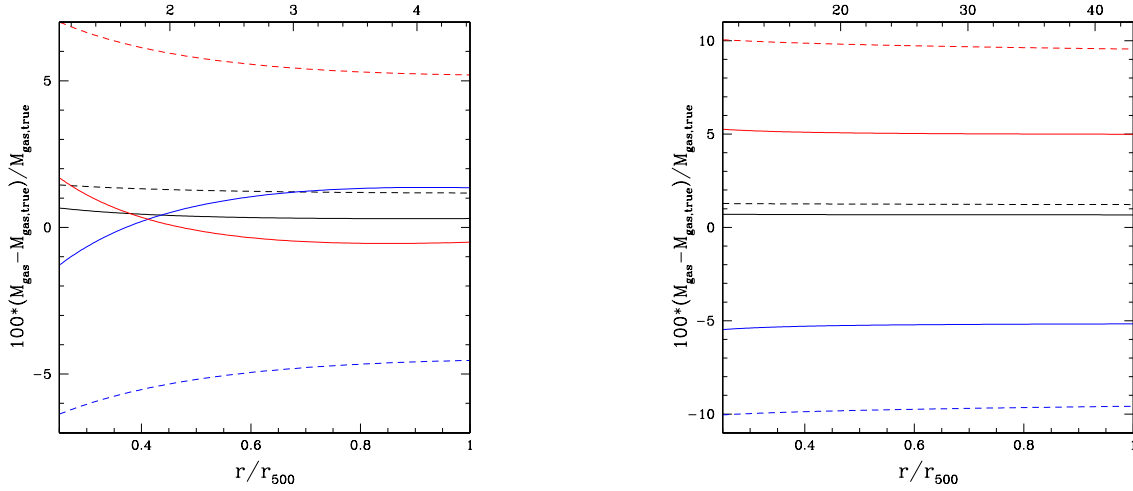


**Figure 9.** Bias of the gas mass plotted as a function of radius between  $0.25 - 1 r_{500}$  for the isothermal (solid lines) and polytropic (dashed lines) NFW-EP (*left panel*) and CORELOG-EP (*right panel*) models for  $q_v = 0.7$  in the potential. Results are displayed for projections down the three principal axes: short (blue), long (red), and intermediate (black). The top axis gives the radius expressed in units of the scale radius for NFW-EP and in units of the core radius for CORELOG-EP.

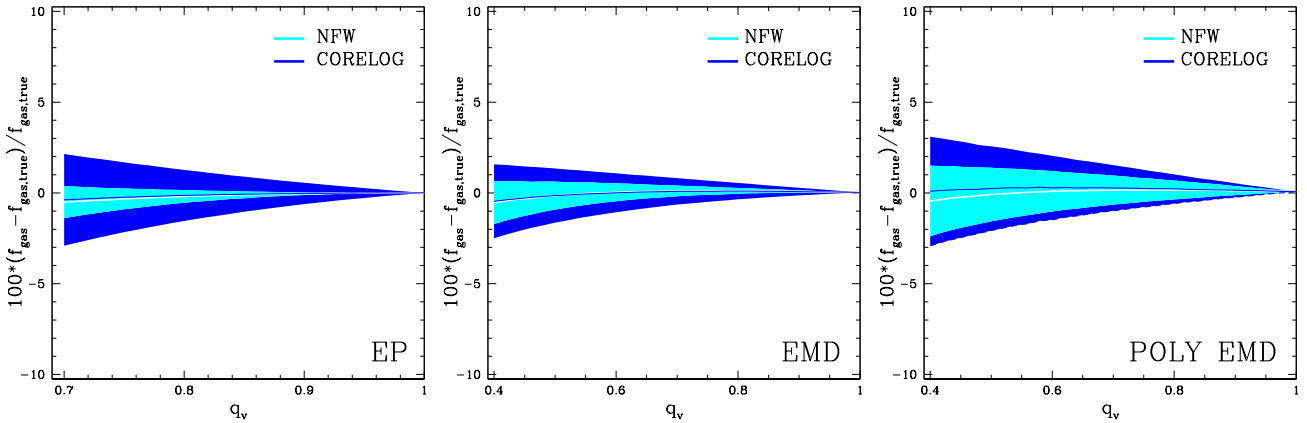


**Figure 10.** Same as Figure 4 except now the bias on the gas fraction is shown.

small:  $\lesssim 1\%$  for EP and about twice as large for EMD. Since the mass bias of an EP does not depend on the temperature profile, the results for the biases for the isothermal and polytropic EPs are identical (not shown). The strong similarity observed between the isothermal and polytropic NFW-EMD models in Fig. 5 indicates that the mass bias of EMDs is also mostly insensitive to the temperature profile. We obtain very similar results for the spheroidal NFW models (Fig. 15).

In contrast, the isothermal CORELOG-EP model possesses essentially zero bias for all projections. This is a consequence of our adopting a large concentration ( $c = 100$ ) so that CORELOG-EP approximates the scale-free logarithmic potential, which we demonstrated in Theorem 9 of Paper 1 (see also Churazov et al. 2008) always has zero mass bias when viewed from any orientation – independent of the temperature profile; i.e., the polytropic CORELOG-EP (not shown) also has zero mass bias for any projection. While not always identically zero, CORELOG-EMD displays a very small range of biases ( $\sigma < 1\%$ ), with the isothermal case having essentially zero average bias. The polytropic CORELOG-EMD model attains an average mass bias of about  $-0.4\%$  for the smallest axial ratio studied ( $q_v = 0.40$ ), though we caution that the polytropic EMD models are the least accurate of all the models investigated (see end of §5.1).

For our fiducial models (excluding the zero-bias CORELOG-EP) the sign of the mass bias is opposite to that found for the concentration parameter (§5.3.1); i.e., projecting down the short axis results in a positive mass bias while the opposite happens when projecting down the long axis. We note, however, that if instead we adopt a smaller value for the concentration (say 10 instead of 100) for the CORELOG-EP model, the behavior reverses for the short and long axis projections. We conclude that the sign of the bias for the mass has a more complex origin than for the concentration.

Our results broadly agree with those obtained by Piffaretti et al. (2003) and Gavazzi (2005) who have previously performed the most extensive examinations of the effects of spherical averaging on the masses of galaxy clusters inferred from X-ray observations. Gavazzi (2005) computed the mass bias as a function of radius for spheroidal, isothermal, NFW-EMD models



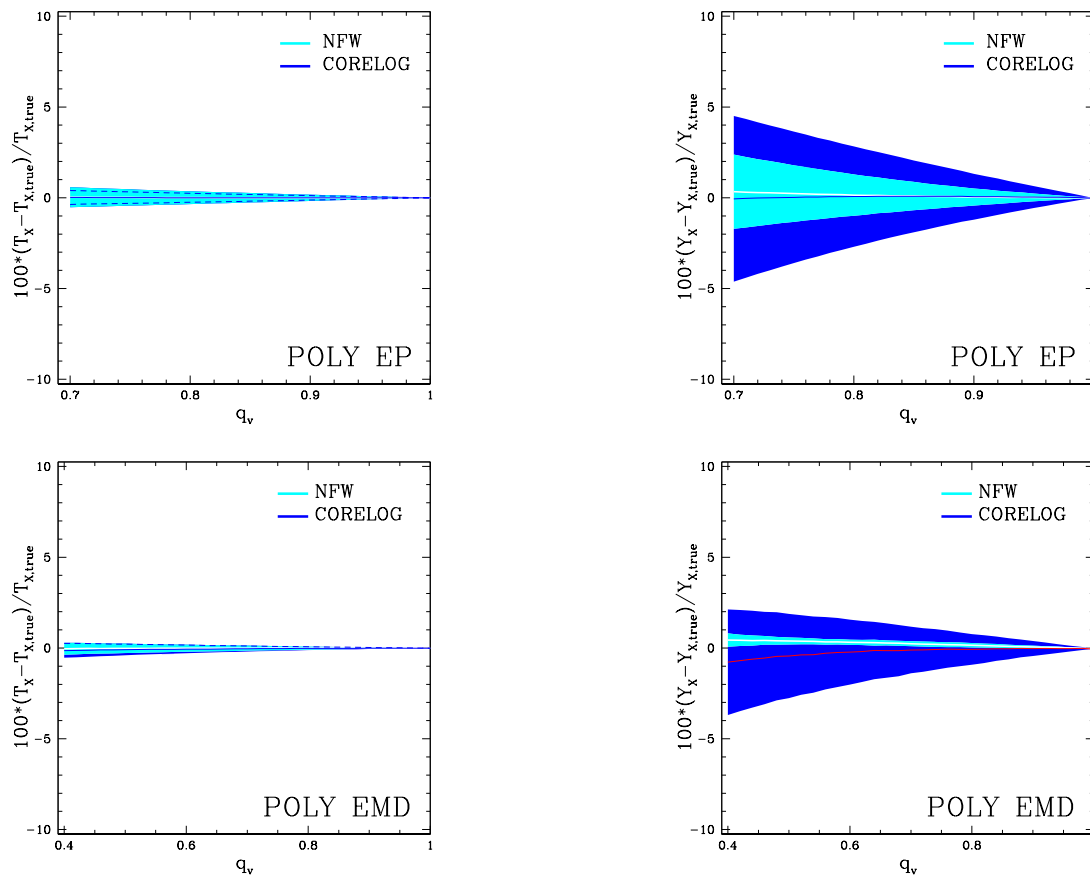


**Figure 11.** Similar to Figure 4 except now the biases on  $T_X$  and  $Y_X$  are shown for the (Top Panels) polytropic EP models and (Bottom Panels) polytropic EMD models. Results for  $Y_X$  for isothermal models are identical to those of the gas mass (Figure 8). For clarity, the blue dashed lines also represent the  $1\sigma$  CORELOG region when it is contained within the  $1\sigma$  NFW region, and the average bias for CORELOG-EMD is denoted by the red solid line.

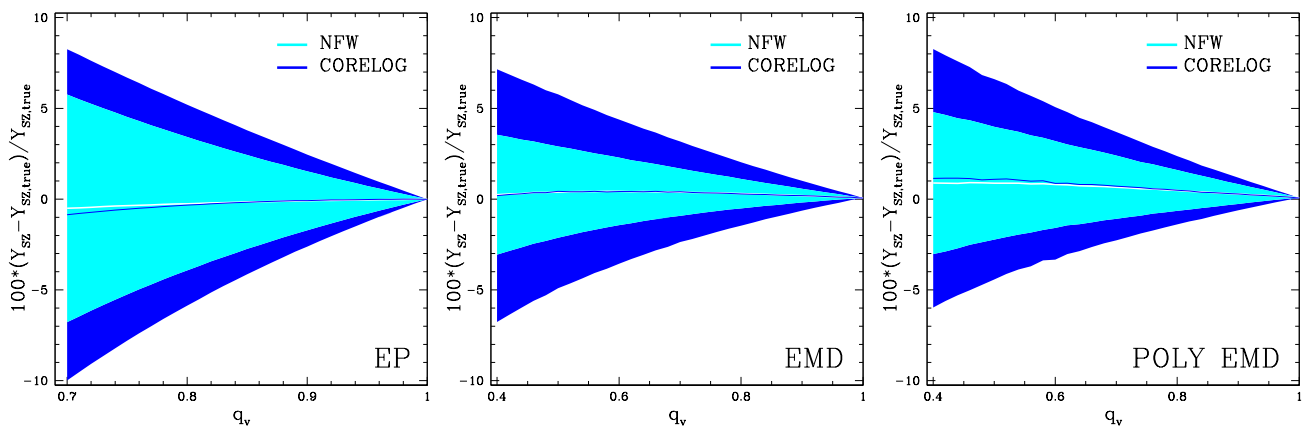


**Figure 12.** Same as Figure 4 except now the bias on the  $Y_{SZ}$  is shown.

viewed down their symmetry axes. Visual inspection of Figure 6 of Gavazzi (2005) reveals that the mass bias for such face-on projections of spheroidal models is generally only a few percent for a radius  $\sim 4r_s \sim r_{500}$ , which agrees reasonably well with our calculations. Piffaretti et al. (2003) instead fitted *ROSAT* X-ray imaging data of ten clusters with an isothermal triaxial  $\beta$  model (i.e., isothermal CORELOG-EP) projected down the intermediate principal axis (i.e., edge-on). They obtained mass biases of magnitude  $\lesssim 4\%$  broadly similar to those of our isothermal NFW-EP model, which provides a more appropriate comparison because our fiducial CORELOG-EP model has a much larger concentration than used by Piffaretti et al. (2003).

When the NFW-EP model is computed within the smaller radius  $r_{2500} \sim 0.46r_{500}$  (Fig. 14), both the mean bias ( $< 0.3\%$ )

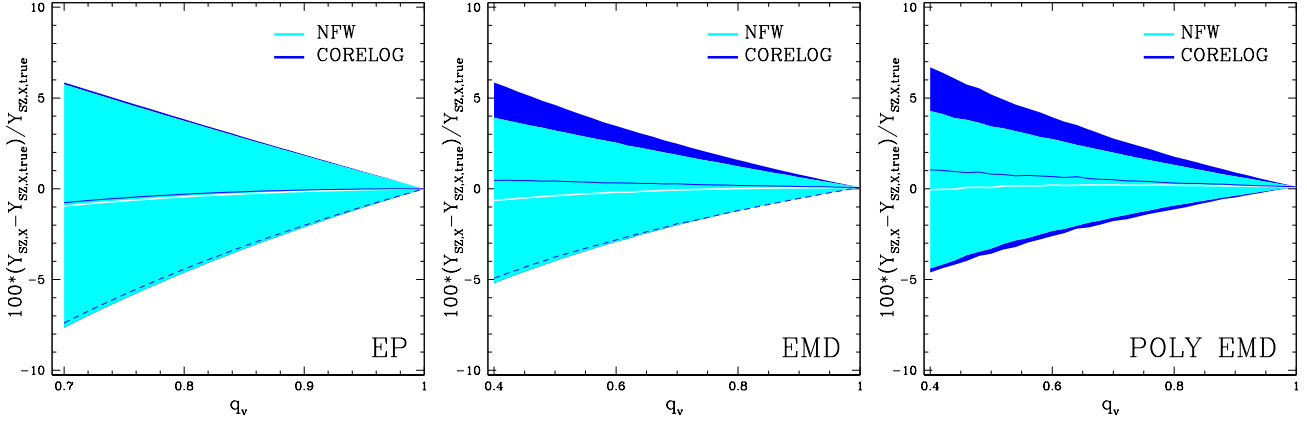


**Figure 13.** Same as Figure 4 except now the bias on the  $Y_{SZ,X}$  is shown.

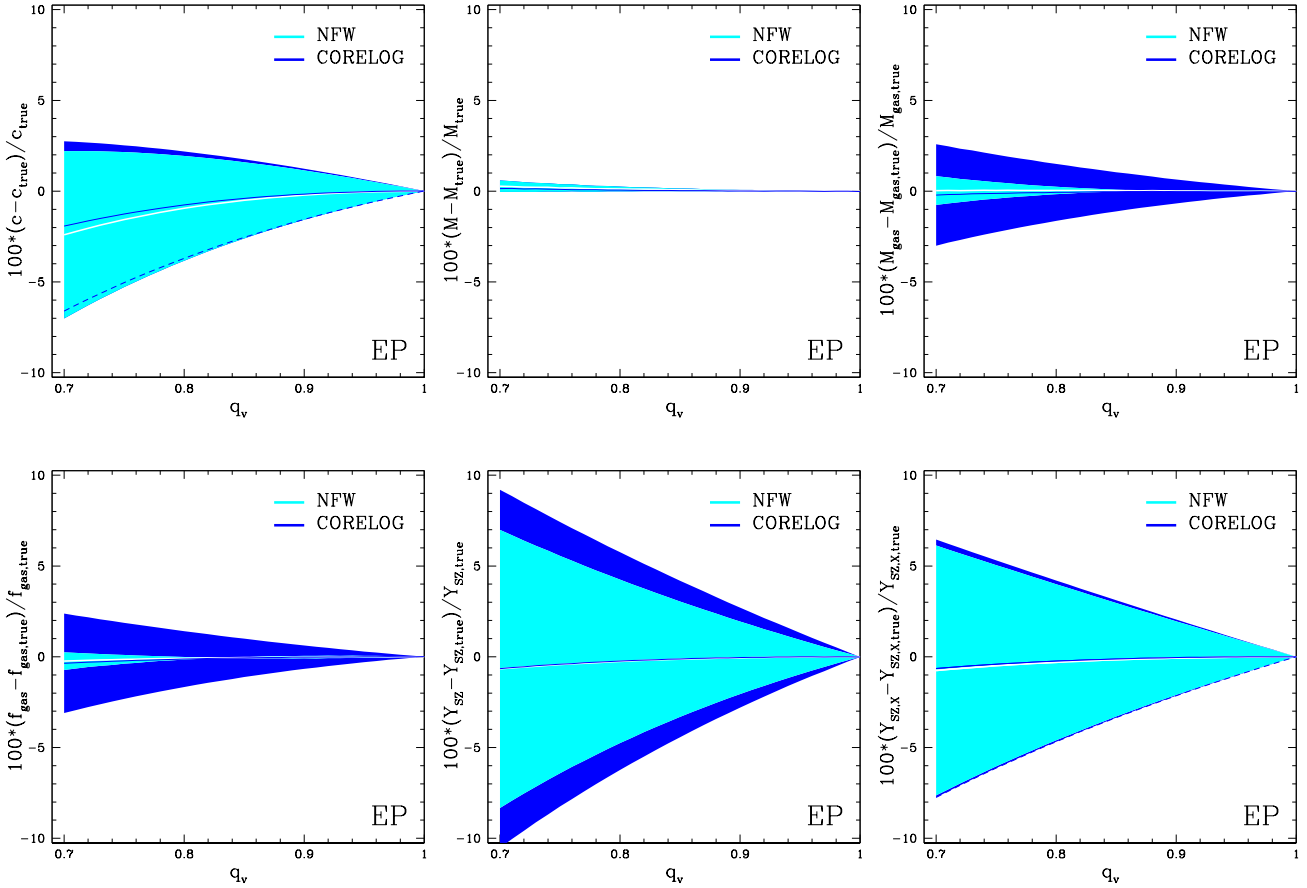


**Figure 14.** Results computed within  $r_{2500}$  for isothermal EP models.

and scatter ( $< 0.3\%$ ) are strikingly smaller than obtained for  $r_{500}$ . Such large changes justify a more detailed examination of the radial dependence of the mass bias for the NFW models. (We do not include CORELOG in this discussion because for the large adopted concentration there are negligible changes in the mass bias with radius.) In Figure 6 we show the radial profile of the mass bias for NFW-EP models with  $q_v = 0.7, 0.9$ . While the projection of the intermediate axis shows little radial variation, the other two projections have larger variations, each of similar magnitude, but of opposite direction. Interestingly, both the short- and long-axis projections cross the line of zero bias at nearly the same radius  $\sim 0.4 r_{500} \sim 1.7 r_s$ . Although we have shown profiles only for two values of  $q_v$ , we find similar results for all  $q_v$  examined.

For comparison, in Figure 7 we show the radial profiles for the mass bias of the NFW-EMD models with  $q_v = 0.4, 0.6$ , which have mass axial ratios at  $r_{500}$  similar to the EPs shown in Figure 6. Although the intermediate-axis projection of

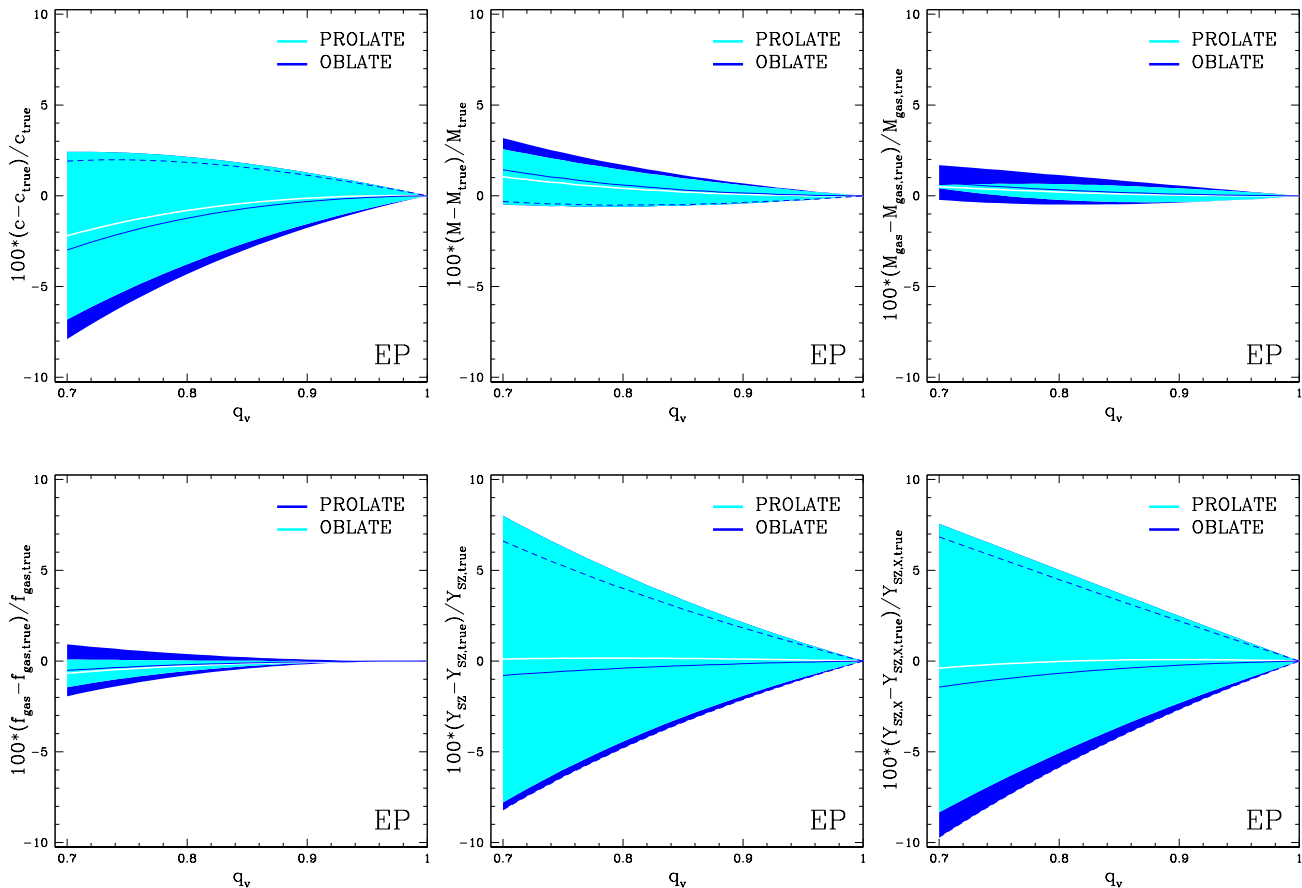


**Figure 15.** Comparison of results for oblate and prolate isothermal NFW-EP models. The solid lines are orientation angle-averaged values, while the shaded regions are the  $1\sigma$  ranges. Note the color coding is reversed for the gas fraction.

the EMDs shows more radial variation than for the EPs, the characteristics of the profiles are very similar. In particular, the bias profiles of the short- and long-axis projections cross the zero bias line at nearly the same radius, this time near  $\sim 0.36 r_{500} \sim 1.5 r_s$ , which also applies to all the EMD models with different  $q_v$  that we investigated. These results are little changed for the polytropic models, consistent with the insensitivity of the global mass bias to temperature gradients discussed above. The largest effects are observed for the  $q_v = 0.4$  EMD model where the crossing of the zero-bias line for the polytropic model occurs closer to  $1.8 r_s$ , but the differences in the biases between the short- and long-axis projections at  $1.8 r_s$  are almost the same as at  $\sim 1.6 r_s$ .

Very similar results are also obtained for spheroidal models, where we have examined short- and long-axis projections, as well as projections along an intermediate direction defined by  $(\theta = 45^\circ, \phi = 45^\circ)$ . We conclude that a useful, general procedure to minimize the mass bias for a galaxy or cluster expected to follow the NFW profile is to measure the mass at a radius  $\approx 0.4 r_{500} \approx 1.7 r_s$ , which should be accurate to within  $\approx 0.5\%$  for any intrinsic axial ratio (and triaxiality), projection orientation, and (isothermal or  $\gamma = 1.2$  polytropic) temperature profile. Since for our models  $r_{2500} \approx 0.46 r_{500}$ , the use of  $r_{2500}$  should also be a very suitable and convenient choice to minimize the orientation mass bias.

As with the global mass bias, we find that our results for the radial variation of the mass bias broadly agree with the face-on projections of spheroidal isothermal NFW-EMD models examined by Gavazzi (2005). From visual inspection of Figure 6 of Gavazzi (2005), his symmetry-axis projections cross the zero-bias line near a radius of  $2 r_s$ , similar to the radius we find minimizes the mass bias for NFW models. Figure 6 of Gavazzi (2005) also shows that the face-on prolate models tend to overestimate the mass within  $\sim 2 r_s$  and underestimate the mass for radii larger than  $\sim 3 r_s$ . The opposite is true for the oblate models. We confirm a similar trend for spheroidal models (not shown).

### 5.3.3 Gas Mass

The mean bias for the gas mass is very similar to that obtained for the total mass. As shown in Fig. 8, the largest bias is  $\approx 1\%$  which occurs for the isothermal NFW-EMD model at  $q_v = 0.40$ , while all the CORELOG models have nearly zero average bias. (We obtain very similar results for the isothermal spheroidal NFW models shown in Fig. 15.) The bias scatter for the

gas mass is generally larger for the CORELOG models, and it exhibits a diversity of model-dependent behavior. For example, the presence of temperature gradients affects the scatter of NFW-EMD and CORELOG-EMD in the opposite manner; i.e., the scatter is larger for the polytropic model compared to the isothermal model for CORELOG and smaller for NFW. In contrast, for EPs the scatter is larger for the polytropic models for both the NFW and CORELOG (not shown). Finally, the sign of the bias in the gas mass for principal-axis projections is also model-dependent; e.g., for isothermal models CORELOG behaves as the concentration while NFW has the opposite behavior (like the total mass).

When the isothermal EPs are computed within the smaller radius  $r_{2500}$ , the mean bias and scatter (Fig. 14) do not change by very much. The most notable difference is that the mean bias for NFW-EP is nearly zero for  $r_{2500}$ . It is also instructive to examine in more detail the radial dependence of the gas mass bias to compare to the total mass. In Figure 9 we display the radial profile of the gas mass bias for projections down the principal axes for the isothermal and polytropic NFW-EP models with  $q_v = 0.7$ . The bias in the gas mass for the isothermal model displays similarities to the bias in the mass, including crossings of the zero-bias line for the short-axis and long-axis projections near radius  $\sim 0.4r_{500}$ . However, the polytropic model has qualitatively different behavior, showing larger biases that do not cross the zero-bias bias line. In fact, the polytropic NFW-EP profile is more similar to profiles of the CORELOG models (right panel of Figure 9) which display very little radial dependence as noted in §5.3.1.

### 5.3.4 Gas Fraction

The behavior of the mean and scatter in the bias of the gas fraction is extremely similar to the gas mass. Generally the magnitude of the mean bias of the gas fraction is the same as, or slightly smaller than, for the gas mass.

### 5.3.5 $T_X$

In Fig. 11 we display results for the emission-weighted temperature integrated over the volume of default radius  $r_{500}$  for polytropic models. Not only do the models all have nearly zero average bias, but overall the bias scatter is the smallest for all the parameters considered. We note that the sign of the bias (for principal-axis projections) for  $T_X$  behaves the same as for the mass.

### 5.3.6 $Y_X$

For isothermal models the biases of  $Y_X$  are identical to the gas mass since  $Y_X = M_{\text{gas}}T_X$ . Given the extremely small bias and scatter for  $T_X$  (§5.3.5), it is unsurprising that even for polytropic models the biases of  $Y_X$  are extremely similar to the gas mass (Fig. 11). Hence, with regard only to the orientation bias of the type considered in our study, we find no significant advantage in terms of either the mean bias or scatter of using  $Y_X$  instead of the gas mass alone.

### 5.3.7 $Y_{SZ}$ and $Y_{SZ,X}$

The integrated Compton-y parameter has a very small ( $\lesssim 1\%$ ) mean bias for all the models considered (Figs. 12, 14, 15). However,  $Y_{SZ}$  does exhibit the largest bias scatter; e.g., for isothermal models,  $\sigma = 6\%$  for NFW-EP and  $\sigma = 9\%$  for CORELOG-EP. Although differing in detail, results for  $Y_{SZ,X} = Y_{SZ}/Y_X$ , are fairly similar to those of  $Y_{SZ}$ . Probably the most noticeable difference is the smaller bias scatter for  $Y_{SZ,X}$  for CORELOG models. These results for  $Y_{SZ,X}$  suggest that for small cluster samples attempts to calibrate the relationship between  $Y_{SZ}$  and  $Y_X$  will encounter significant intrinsic scatter owing to orientation bias. Fortunately, our models indicate that by averaging over a large number of randomly oriented clusters this source of systematic error can be reduced to less than one percent. Current observations (e.g., Andersson et al. 2011; Planck Collaboration et al. 2011) are consistent with larger intrinsic scatter than that associated with the orientation bias on  $Y_{SZ,X}$  that we have computed.

## 5.4 Comment on the Assumption of Random Orientations

Our analysis assumes that clusters are randomly oriented to the observer’s line of sight. However, in an X-ray flux-limited sample there may be a bias toward selecting clusters viewed down their major axis, since this orientation gives rise to the highest central surface brightness in an ellipsoidal cluster. As mentioned in §1, we have assumed “ideal measurements” of galaxy clusters, which in this context means we have assumed a volume-limited cluster sample free of such observational biases. Similarly, the gravitational fields generated by large-scale structures likely establish weak cluster alignments on  $\sim 40$  Mpc scales (e.g., Paz et al. 2011, and references therein). By assuming a sample volume much larger than this scale, we expect that small deviations from random orientations due to this effect impact our calculations less than the systematic

differences observed between the different models explored in our paper; e.g., EP vs. EMD, NFW vs. CORELOG, isothermal vs. polytropic. Cosmological N-body simulations are required to investigate this further.

## 6 CONCLUSIONS

This is the second of two papers investigating the spherical averaging of ellipsoidal galaxy clusters (and massive elliptical galaxies) in the context of X-ray and SZ studies. In Paper 1 we present analytical formulas describing both the deprojection and spherical averaging of EPs. In the present study we quantify the mean bias and scatter in cluster observables (e.g., mass) resulting from spherical averaging in the following sense. We associate “true” spherically averaged values with those computed from direct spherical averaging of the true three-dimensional cluster, as is done typically in theoretical studies. To obtain the observer’s perspective, we initially fill up the ellipsoidal cluster’s potential well with hot ICM by assuming hydrostatic equilibrium. The X-ray emission from this ellipsoidal model is projected onto the sky for a particular orientation. From this point onward the hypothetical observer treats the cluster as spherical; i.e., the observer circularly averages the X-ray image and temperature map and deprojects each of them assuming spherical symmetry. We use these profiles to compute “observed” spherically averaged quantities. By comparing the “true” and “observed” spherically averaged quantities we compute the bias arising from the inconsistent spherical averaging procedures.

Our study extends previous work (e.g., Piffaretti et al. 2003; Gavazzi 2005) on this topic in a few key respects. Of most importance, unlike previous studies that examined biases using only a single projection direction, we compute statistical orientation bias distributions for each cluster parameter. This allows us to present the first calculations of the orientation-averaged bias and scatter in cluster properties derived from X-ray and SZ studies. (Note that although we find that the parameter bias distributions are non-gaussian, because they are also centrally peaked it is nevertheless useful for our present investigation to describe them using the mean and standard deviation.) We also employ a more diverse set of cluster models than considered in previous individual studies. First, we consider clusters having a constant shape or one that changes with radius – in either the mass or ICM; i.e., both EPs and EMDs. Second, our fiducial models are maximally triaxial (triaxiality parameter,  $T = 0.5$ ), though we also examine both oblate ( $T = 0$ ) and prolate ( $T = 1$ ) spheroids for comparison. Second, we examine gravitational potentials corresponding either to the NFW profile or a (nearly scale-free) logarithmic potential. Third, for the ICM we consider both isothermal models and (polytropic) models with temperature gradients. Finally, we examine the biases for several parameters: concentration, (total) mass, gas mass, gas fraction, emission-weighted temperature ( $T_X$ ),  $Y_X$ , integrated Compton-y parameter ( $Y_{SZ}$ ), and the ratio  $Y_{SZ,X} = Y_{SZ}/Y_X$ .

We find that substantial biases can result from different viewing orientations, where  $Y_{SZ}$  and the concentration have the largest scatter (as large as  $\sigma \sim 10\%$  for  $Y_{SZ}$ ) and  $T_X$  has the smallest ( $\sigma \lesssim 0.5\%$ ). As expected, the biases of largest magnitude occur for the flattest models; i.e.,  $q_v = 0.7$  for EPs and  $q_v = 0.4$  for EMDs. Because the orientation bias of  $T_X$  displays such a small scatter, we find that the scatters for  $Y_X$  and  $M_{\text{gas}}$  are virtually the same (as are their mean biases). Hence, spherical averaging of ellipsoidal clusters has essentially the same effect on  $Y_X$  as it does on  $M_{\text{gas}}$ . We conclude in light of this that the smaller scatter for  $Y_X$  obtained from cosmological hydrodynamical simulations (Kravtsov et al. 2006) might be attributed to effects not considered in our study, especially deviations from ellipsoidal geometry and hydrostatic equilibrium.

Although the mean biases are small and almost always  $< 1\%$ , the flattest models generally have a significant non-zero bias; i.e., typically orientation angle averaging does not completely eliminate projection biases. The mean biases of largest magnitude occur for the concentration parameter  $\sim -3\%$ , while  $T_X$  always has nearly zero mean bias. Despite  $Y_{SZ}$  having the largest scatter, we find that its mean bias is always  $\lesssim 1\%$ . Finally, the masses of the nearly scale-free CORELOG models – both EP and EMD – exhibit very small (or zero) mean bias and scatter.

Orientation bias can generate significant scatter (up to  $\sigma \sim 8\%$  for the flattest systems) in the relationship between  $Y_{SZ}$  and  $Y_X$  (as expressed by  $Y_{SZ,X}$ ). This will be a significant source of uncertainty for measurements of the  $Y_{SZ} - Y_X$  relation using small cluster samples. Fortunately, since the mean bias for  $Y_{SZ,X}$  is small ( $\sigma \lesssim 1\%$ ), for large enough cluster samples the orientation bias can be reduced below one percent.

Our results do not change significantly over a wide range in halo mass ( $10^{12} - 10^{15} M_\odot$ ) spanning massive elliptical galaxies to galaxy clusters. However, we do observe an interesting trend in the radial profile of the orientation bias for the mass for a cluster that follows the NFW profile. The scatter in the mass bias attains a minimum near the radius  $0.4 r_{500} \approx 1.7 r_s \approx r_{2500}$ . Consequently, considering the effect of orientation bias, the mass computed at this radius is always within  $\approx 0.5\%$  of the true value for any orientation for all of our models. For comparisons between a small number of clusters, it is useful to quote masses at  $r_{2500}$  to minimize the orientation bias.

It is important to recognize that even though the  $1\sigma$  scatter of the orientation bias for any parameter we have investigated is  $\lesssim 10\%$ , the scatter is not small relative to other sources of systematic error. Take for example the gas fraction of the fossil group/cluster RXJ 1159+5531 for which we provide a detailed systematic error budget from a combined *Chandra* and *Suzaku* analysis (see Table 2 of Humphrey et al. 2011). The systematic errors reported on the gas fraction computed within  $r_{500}$  are  $\sim 3\%$  which is very similar to the  $1\sigma$  scatter in the orientation bias for the flattest ellipsoids (Fig. 10). Hence, orientation

bias is not negligible compared to other effects, and this is especially so in a fossil system like RXJ 1159+5531 where there is evidence that the hydrostatic equilibrium approximation is accurate.

To facilitate the accounting for orientation bias in X-ray and SZ cluster studies, we provide cubic polynomial approximations to the mean bias and  $1\sigma$  scatter as a function of axial ratio  $q_v$  for each parameter for the (maximally triaxial) isothermal NFW models (Table 1). These can be consulted to estimate the typical range of orientation bias for a given parameter and to construct a prior probability distribution for Bayesian studies. In the latter case, to average over  $q_v$  for a given halo mass the probability distribution for  $\Lambda$ CDM halos by Jing & Suto (2002) can be employed directly for the NFW-EMD model.

## ACKNOWLEDGMENTS

We gratefully acknowledge partial support from the National Aeronautics and Space Administration under Grant No. NNX10AD07G issued through the Astrophysics Data Analysis Program.

## REFERENCES

- Allen S. W., Evrard A. E., Mantz A. B., 2011, *ARA&A*, 49, 409
- Allgood B., Flores R. A., Primack J. R., Kravtsov A. V., Wechsler R. H., Faltenbacher A., Bullock J. S., 2006, *MNRAS*, 367, 1781
- Andersson K., Benson B. A., Ade P. A. R., Aird K. A., Armstrong B., Bautz M., Bleem L. E., Brodwin M., Carlstrom J. E., Chang C. L., Crawford T. M., Crites A. T., et al. 2011, *ApJ*, 738, 48
- Arnaud K. A., 1996, in Jacoby G. H., Barnes J., eds, *Astronomical Data Analysis Software and Systems V* Vol. 101 of *Astronomical Society of the Pacific Conference Series*, XSPEC: The First Ten Years. p. 17
- Arnaud M., 2005, in F. Melchiorri & Y. Rephaeli ed., *Background Microwave Radiation and Intracluster Cosmology X-ray observations of clusters of galaxies*. p. 77
- Arnaud M., Pointecouteau E., Pratt G. W., 2005, *A&A*, 441, 893
- Arnaud M., Pointecouteau E., Pratt G. W., 2007, *A&A*, 474, L37
- Bailin J., Steinmetz M., 2005, *ApJ*, 627, 647
- Binney J., 1981, *MNRAS*, 196, 455
- Binney J., Strimpele O., 1978, *MNRAS*, 185, 473
- Binney J., Tremaine S., 2008, *Galactic Dynamics: Second Edition*. Princeton University Press
- Borgani S., Finoguenov A., Kay S. T., Ponman T. J., Springel V., Tozzi P., Voit G. M., 2005, *MNRAS*, 361, 233
- Brighenti F., Mathews W. G., 2001, *ApJ*, 553, 103
- Buote D. A., Canizares C. R., 1994, *ApJ*, 427, 86
- Buote D. A., Canizares C. R., 1996a, *ApJ*, 457, 177
- Buote D. A., Canizares C. R., 1996b, *ApJ*, 457, 565
- Buote D. A., Gastaldello F., Humphrey P. J., Zappacosta L., Bullock J. S., Brighenti F., Mathews W. G., 2007, *ApJ*, 664, 123
- Buote D. A., Humphrey P. J., 2011, *MNRAS*, in press (arXiv:1109.6921)
- Buote D. A., Humphrey P. J., 2012, in D.-W. Kim & S. Pellegrini ed., *Astrophysics and Space Science Library* Vol. 378 of *Astrophysics and Space Science Library*, *Dark Matter in Elliptical Galaxies*. p. 235
- Cavaliere A., Fusco-Femiano R., 1976, *A&A*, 49, 137
- Chandrasekhar S., 1987, *Ellipsoidal figures of equilibrium*
- Churazov E., Forman W., Vikhlinin A., Tremaine S., Gerhard O., Jones C., 2008, *MNRAS*, 388, 1062
- Debattista V. P., Moore B., Quinn T., Kazantzidis S., Maas R., Mayer L., Read J., Stadel J., 2008, *ApJ*, 681, 1076
- Evans N. W., 1993, *MNRAS*, 260, 191
- Evrard A. E., Metzler C. A., Navarro J. F., 1996, *ApJ*, 469, 494
- Fabian A. C., Hu E. M., Cowie L. L., Grindlay J., 1981, *ApJ*, 248, 47
- Fabricant D., Rybicki G., Gorenstein P., 1984, *ApJ*, 286, 186
- Franx M., Illingworth G., de Zeeuw T., 1991, *ApJ*, 383, 112
- Gavazzi R., 2005, *A&A*, 443, 793
- Grego L., Carlstrom J. E., Joy M. K., Reese E. D., Holder G. P., Patel S., Cooray A. R., Holzappel W. L., 2000, *ApJ*, 539, 39
- Henry J. P., 2003, in S. Bowyer & C.-Y. Hwang ed., *Astronomical Society of the Pacific Conference Series* Vol. 301 of *Astronomical Society of the Pacific Conference Series*, *Evolution of the X-Ray Properties of Clusters of Galaxies*. p. 5
- Humphrey P. J., Buote D. A., Brighenti F., Flohic H. M. L. G., Gastaldello F., Mathews W. G., 2011, *ArXiv e-prints* (1106.3322)

- Jing Y. P., Suto Y., 2002, *ApJ*, 574, 538
- Kassiola A., Kovner I., 1993, *ApJ*, 417, 450
- Kazantzidis S., Kravtsov A. V., Zentner A. R., Allgood B., Nagai D., Moore B., 2004, *ApJ*, 611, L73
- Krause E., Pierpaoli E., Dolag K., Borgani S., 2011, *ArXiv e-prints*
- Kravtsov A. V., Vikhlinin A., Nagai D., 2006, *ApJ*, 650, 128
- Kriss G. A., Cioffi D. F., Canizares C. R., 1983, *ApJ*, 272, 439
- Lewis A. D., Buote D. A., Stocke J. T., 2003, *ApJ*, 586, 135
- Macciò A. V., Dutton A. A., van den Bosch F. C., 2008, *MNRAS*, 391, 1940
- McCarthy I. G., Babul A., Bower R. G., Balogh M. L., 2008, *MNRAS*, 386, 1309
- McCarthy I. G., Schaye J., Ponman T. J., Bower R. G., Booth C. M., Dalla Vecchia C., Crain R. A., Springel V., Theuns T., Wiersma R. P. C., 2010, *MNRAS*, 406, 822
- McLaughlin D. E., 1999, *AJ*, 117, 2398
- Merritt D., Fridman T., 1996, *ApJ*, 460, 136
- Merritt D., Navarro J. F., Ludlow A., Jenkins A., 2005, *ApJ*, 624, L85
- Muñoz-Cuartas J. C., Macciò A. V., Gottlöber S., Dutton A. A., 2011, *MNRAS*, 411, 584
- Nagai D., Lau E. T., 2011, *ApJ*, 731, L10
- Nagai D., Vikhlinin A., Kravtsov A. V., 2007, *ApJ*, 655, 98
- Navarro J. F., Frenk C. S., White S. D. M., 1997, *ApJ*, 490, 493
- Navarro J. F., Hayashi E., Power C., Jenkins A. R., Frenk C. S., White S. D. M., Springel V., Stadel J., Quinn T. R., 2004, *MNRAS*, 349, 1039
- Ostriker J. P., Bode P., Babul A., 2005, *ApJ*, 634, 964
- Paz D. J., Sgró M. A., Merchán M., Padilla N., 2011, *MNRAS*, 414, 2029
- Piffaretti R., Jetzer P., Schindler S., 2003, *A&A*, 398, 41
- Piffaretti R., Valdarnini R., 2008, *A&A*, 491, 71
- Planck Collaboration Ade P. A. R., Aghanim N., Arnaud M., Ashdown M., Aumont J., Baccigalupi C., Balbi A., Banday A. J., Barreiro R. B., et al. 2011, *A&A*, 536, A11
- Pratt G. W., Arnaud M., Piffaretti R., Böhringer H., Ponman T. J., Croston J. H., Voit G. M., Borgani S., Bower R. G., 2010, *A&A*, 511, A85
- Rasia E., Ettori S., Moscardini L., Mazzotta P., Borgani S., Dolag K., Tormen G., Cheng L. M., Diaferio A., 2006, *MNRAS*, 369, 2013
- Romeo A. D., Sommer-Larsen J., Portinari L., Antonuccio-Delogu V., 2006, *MNRAS*, 371, 548
- Sanders J. S., Fabian A. C., Smith R. K., 2011, *MNRAS*, 410, 1797
- Sarazin C. L., 1986, *Reviews of Modern Physics*, 58, 1
- Schuecker P., 2005, in S. Röser ed., *Reviews in Modern Astronomy Vol. 18 of Reviews in Modern Astronomy, New Cosmology with Clusters of Galaxies*. pp 76–105
- Schuecker P., Finoguenov A., Miniati F., Böhringer H., Briel U. G., 2004, *A&A*, 426, 387
- Shaw L. D., Holder G. P., Bode P., 2008, *ApJ*, 686, 206
- Simionescu A., Allen S. W., Mantz A., Werner N., Takei Y., Morris R. G., Fabian A. C., Sanders J. S., Nulsen P. E. J., George M. R., Taylor G. B., 2011, *Science*, 331, 1576
- Smith R. K., Brickhouse N. S., Liedahl D. A., Raymond J. C., 2001, *ApJ*, 556, L91
- Takahashi T., 2011, in J.-U. Ness & M. Ehle ed., *The X-ray Universe 2011, Presentations of the Conference held in Berlin, Germany, 27-30 June 2011*. Available online at: [http://xmm.esac.esa.int/external/xmm\\_science/workshops/2011symposium/](http://xmm.esac.esa.int/external/xmm_science/workshops/2011symposium/), p.433 *The ASTRO-H Mission*. p. 433
- Tozzi P., 2007, in L. Papantonopoulos ed., *The Invisible Universe: Dark Matter and Dark Energy Vol. 720 of Lecture Notes in Physics*, Berlin Springer Verlag, *Cosmological Parameters from Galaxy Clusters: An Introduction*. p. 125
- Tozzi P., Norman C., 2001, *ApJ*, 546, 63
- Trinchieri G., Fabbiano G., Canizares C. R., 1986, *ApJ*, 310, 637
- Tsai J. C., Katz N., Bertschinger E., 1994, *ApJ*, 423, 553
- Urban O., Werner N., Simionescu A., Allen S. W., Böhringer H., 2011, *MNRAS*, 414, 2101
- Vazza F., Brunetti G., Gheller C., Brunino R., Brügggen M., 2011, *A&A*, 529, A17
- Voit G. M., 2005, *Reviews of Modern Physics*, 77, 207
- Voit G. M., Bryan G. L., Balogh M. L., Bower R. G., 2002, *ApJ*, 576, 601
- Voit G. M., Kay S. T., Bryan G. L., 2005, *MNRAS*, 364, 909
- White D. A., Fabian A. C., Allen S. W., Edge A. C., Crawford C. S., Johnstone R. M., Stewart G. C., Voges W., 1994, *MNRAS*, 269, 589
- White M., Hernquist L., Springel V., 2002, *ApJ*, 579, 16
- Younger J. D., Bryan G. L., 2007, *ApJ*, 666, 647

Zaroubi S., Squires G., Hoffman Y., Silk J., 1998, *ApJ*, 500, L87